5-2014

Resolving the Temporal-Spatial Ambiguity With the Auroral Spatial Structures Probe

Daniel Farr
Utah State University

RESOLVING THE TEMPORAL-SPATIAL AMBIGUITY WITH THE AURORAL SPATIAL STRUCTURES PROBE

by

Daniel Farr

A thesis submitted in partial fulfillment
of the requirements for the degree

of

MASTER OF SCIENCE

in

Electrical Engineering

Approved:

Dr. Charles Swenson Major Professor	Dr. Jacob Gunther Committee Member
Dr. Todd Moon Committee Member	Dr. Mark R. McLellan Vice President for Research and Dean of the School of Graduate Studies

UTAH STATE UNIVERSITY
Logan, Utah

2014

Abstract

Resolving the Temporal-Spatial Ambiguity with the Auroral Spatial Structures Probe

by

Daniel Farr, Master of Science

Utah State University, 2014

Major Professor: Dr. Charles Swenson
Department: Electrical and Computer Engineering

The Auroral Spatial Structures Probe (ASSP) is a National Aeronautics and Space Administration (NASA) sounding rocket mission to measure small scale temporal and spatial variations in the Earth's electric and magnetic fields during breakup aurora conditions. Multiple time-separated measurements of the same spatial location must be made in order to resolve the temporal-spatial ambiguity. ASSP achieves multipoint measurements by ejecting a constellation of six subpayloads from the main payload. This thesis develops a method for identifying the optimal ejection vector, propose an automated test plan for calibrating the seven payloads, and discuss several challenges relating to the interpretation of ASSP data.

(63 pages)

Public Abstract

Resolving the Temporal-Spatial Ambiguity with the Auroral Spatial Structures Probe

by

Daniel Farr, Master of Science

Utah State University, 2014

Major Professor: Dr. Charles Swenson
Department: Electrical and Computer Engineering

The behavior of the electric and magnetic fields in the upper atmosphere of the Earth is scientifically interesting but difficult to study, since balloons and aircraft are unable to fly high enough to measure it directly. Sounding rockets, which make a one-time flight carrying instruments that measure the environment around them, have been successfully used to study the upper atmosphere. As the rocket flies through the upper atmosphere, it radios down data about the environment. When scientists on the ground use this data to construct a picture of the upper atmosphere, they run into a problem: the fields reported by the rocket change over time, but it is not clear whether this is because these fields are actually changing in time, or just because the rocket has moved to a different place where the fields are different. This inability to determine whether changes are happening in time or space is called the temporal-spatial ambiguity.

This thesis describes the Auroral Spatial Structures Probe (ASSP), a sounding rocket mission that attempts to resolve the temporal-spatial ambiguity by using multiple payloads flying in formation. Several payloads will pass through and measure the same point in space one after another, which will enable us to see how the fields are changing over time.

Acknowledgments

Many people worked on the sounding rocket mission of which the work described here is only a small part. This thesis would not have been possible without the efforts of many Utah State University students at the Space Dynamics Lab, or those of said lab's National Aeronautics and Space Administration (NASA) collaborators. Ernest Bowden and Mike Disbrow at NASA Wallops flight facility should especially be thanked for their advice and support.

I owe a great debt to my advisor, Charles Swenson. It would not be much of an exaggeration to say that all the work reported here was really, to a greater or lesser degree, done in collaboration with him.

Daniel Farr

Contents

Page

Abstract . . . . . **iii**

Public Abstract . . . . . **iv**

Acknowledgments . . . . . **v**

List of Tables . . . . . **viii**

List of Figures . . . . . **ix**

1 Introduction **1**
1.1 Previous Missions 5
1.2 ASSP Payload and Instrumentation 7
1.3 Thesis Overview 11

2 Ejection Angle Optimization **13**
2.1 Objective 13
2.1.1 Motion in a Non-Inertial Frame of Reference 13
2.1.2 The Parameter to be Optimized 14
2.2 Implementation 18
2.2.1 Main Payload Dispersion 18
2.2.2 Architecture 20
2.2.3 ACS Pointing Objective 20
2.3 Results 24

3 Instrument Calibration Theory **27**
3.1 Electric Field Probe 27
3.2 Magnetometer 29
3.3 Trimming the Magnetometer 32
3.4 Langmuir Probe 34

4 Instrument Testing **36**
4.1 Automation 36
4.1.1 Testing Superbox 37
4.1.2 White Noise Source 38
4.2 Test Plan 42
4.2.1 E-field Gain and Offset 42
4.2.2 E-field Frequency Response 42
4.2.3 E-field Input Resistance 44
4.2.4 E-field Spectrometer Frequency Response 44
4.2.5 E-field Spectrometer White Noise Response 44

4.2.6 Magnetometer Gain and Offset 45
4.2.7 Magnetometer Frequency Response 45
4.2.8 Langmuir Probe Gain and Linearity 45
4.2.9 Langmuir Probe Precision Gain and Linearity 46
4.2.10 Langmuir Probe Frequency Response 46

5 Future Tasks 48

References 50

Appendix 51

List of Tables

Table Page

1.1 Science objectives to measurement requirements. 8

4.1 Current steps for Langmuir probe testing. 46

List of Figures

Figure		Page
1.1	ASSP passing over the aurora.	3
1.2	Resolved temporal and spatial scales.	4
1.3	Subpayload ejection directions.	5
1.4	Mission timeline.	6
1.5	An ASSP subpayload.	8
1.6	The ASSP main payload.	9
1.7	Subpayload telemetry.	10
1.8	Main payload telemetry.	10
1.9	The ASSP main payload before ejection and boom deployment.	11
1.10	Ejection hardware testing.	12
2.1	Two payloads passing through the same flux tube.	15
2.2	Main and subpayload 1 trajectories projected to a common altitude.	17
2.3	Main and subpayload 1 trajectories with exaggerated point-to-point separation.	17
2.4	Map showing 1, 2, and 3σ main payload impact range (courtesy of NASA).	19
2.5	Matlab script dependency flowchart.	21
2.6	Subpayload 1 polynomial coefficients.	23
2.7	Actual target versus polynomial approximation.	23
2.8	Crosstrack separation between the main payload and subpayload 1.	25
2.9	Crosstrack separation between the main payload and each subpayload.	26
2.10	Consequences of error in ejection angle.	26
3.1	Model of the E-field instrument.	27

3.2 Model of the magnetometer. 30

3.3 The three magnetometer bridges. 33

3.4 Model of the Langmuir probe. 34

4.1 Testing physical setup. 37

4.2 Superbox high-level schematic. 39

4.3 Photograph of a built superbox. 39

4.4 White noise source circuit. 40

4.5 Noise through successive gain stages. 41

4.6 White noise circuit PCB layout. 43

4.7 ASSP thermal test plan (courtesy of Julio Martin Hidalgo). 43

Chapter 1

Introduction

The sun is continually streaming plasma and radiation particles out into space in what is known as the solar wind. Magnetic field lines from the sun's surface become embedded in the outward flowing solar wind resulting in an interplanetary magnetic field. Emitted in all directions, the presence of this wind and field is essentially constant but its direction, density, and speed can vary. The solar wind buffets the Earth, creating interesting effects such as the aurora and geomagnetic storms. Earth's magnetic field serves as a shield to the streaming plasma of the solar wind, redirecting the material around the planet. The force of the wind interacts with the Earths magnetic field so that it is compressed inward on the sun-side and stretched outward on the night side. This region, dominated by the Earths magnetic field, is called the magnetosphere and on its surface the kinetic energy of the solar wind is converted to electromagnetic energy resulting in electrical potentials and currents that flow within the Earths magnetosphere and ionosphere. Much of this energy is directed into the high latitude regions of the planet where the aurora is observed. The rate of energy input in this auroral region is modulated by the interplanetary magnetic field, and by the fact that the magnetosphere can store energy in one region for a later and often abrupt or explosive release in what is called a geomagnetic storm.

The electromagnetic energy input from the magnetosphere into the ionosphere at high latitudes varies both temporally and spatially across the Earths polar regions due to the changing solar wind-magnetosphere interactions. This energy can be characterized by the Poynting flux, which can be determined from observations of the electric and magnetic field. Conservation of energy means that the Poynting flux is equal to the sum of the processes—primarily driven currents and auroral particle heating—by which energy is deposited within the high latitude ionosphere. Auroral particle heating results in the majestic visual aurora

with its thin waving curtains of light. Currents, which are not visible and for which the spatial structure is largely unknown are thought to deposit up to ten times the energy of auroral particles.

The Auroral Spatial Structures Probe (ASSP) is a National Aeronautics and Space Administration (NASA) sounding rocket mission designed to understand the contributions of small spatial scale and rapid temporal scale fluctuations of electric fields and currents that deposit energy in the auroral region. It will launch from Poker Flat Research Range in Alaska in January 2015. Figure 1.1 shows the region the mission will cover, as well as the location of the auroral activity to be observed. The objective is to investigate the small-scale spatial and temporal variability in the E-field that is known to contribute significantly to the overall heating at high latitudes. These fluctuations have long been observed by previous sounding rocket and satellite missions, but the basic question of what portion of the observed signal variation is a temporal change and what portion is due to flying through a varying spatial structure has not been addressed. In other words, time-space separated observations at small scales have not been made yet: satellites are able to sample the fields at small spatial scales (limited by their sampling rate and the great speed of the vehicle) but are unable to examine rapid temporal changes since it takes them more than an hour to orbit the Earth and return to sample a location again. Ground-based observation platforms are able to make much faster observations, with time resolution as fast as about one minute, but are unable to resolve spatial features smaller than tens of kilometers. Figure 1.2 summarizes the the temporal and spatial scales resolved by programs up until now, as well as the region ASSP proposes to examine.

Sounding rockets, which fly a suborbital trajectory and make measurements in situ, are able to make fast measurements at small spatial scales, but there is a temporal-spatial ambiguity in the data they return. The problem is easier to visualize in two dimensions. Imagine a small pond, with waves propagating across the surface in response to some disturbance. If a single sensor were to move over the surface measuring the height of the water just at its own location, would that information allow one to develop a realistic

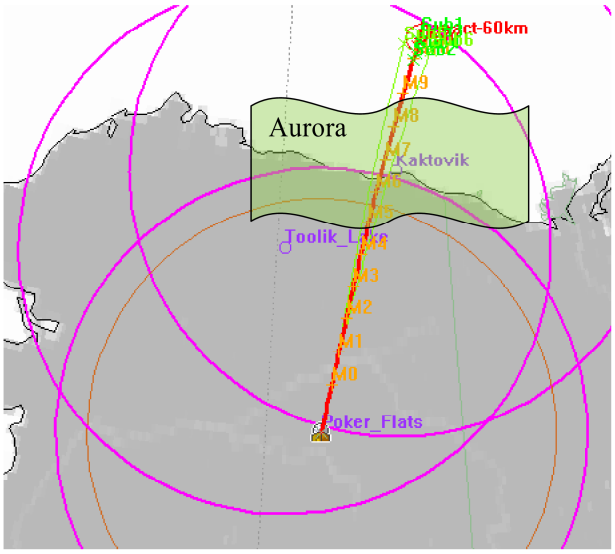

Fig. 1.1: ASSP passing over the aurora.

picture of the waves on the water?

The answer is no. A sensor moving in the same direction as fast-moving waves would see the same thing as one moving in the opposite direction of slow-moving waves. It is impossible to tell the difference between amplitude changes the sensor is seeing due to its own motion and changes due to the environment changing around it. This uncertainty is called the temporal-spatial ambiguity. It would be nice to be able to either stay in one place and let the waves move past the sensor, or move across the surface so quickly that the waves do not have time to change during transit, since neither of these sensing strategies will suffer from a temporal-spatial ambiguity.

The electromagnetic fields in the space environment are analogous to the water surface under discussion, although much more complicated and 3d rather than 2d. It is impossible to fly a sounding rocket either fast enough that it completes its path before the electromagnetic fields have time to change or slow enough that it can be approximated as being still while the environment changes around it. So how can the temporal-spatial ambiguity be resolved?

ASSP attempts to resolve the temporal-spatial ambiguity by using multiple payloads to sample the same location multiple times, and also sample multiple locations at the

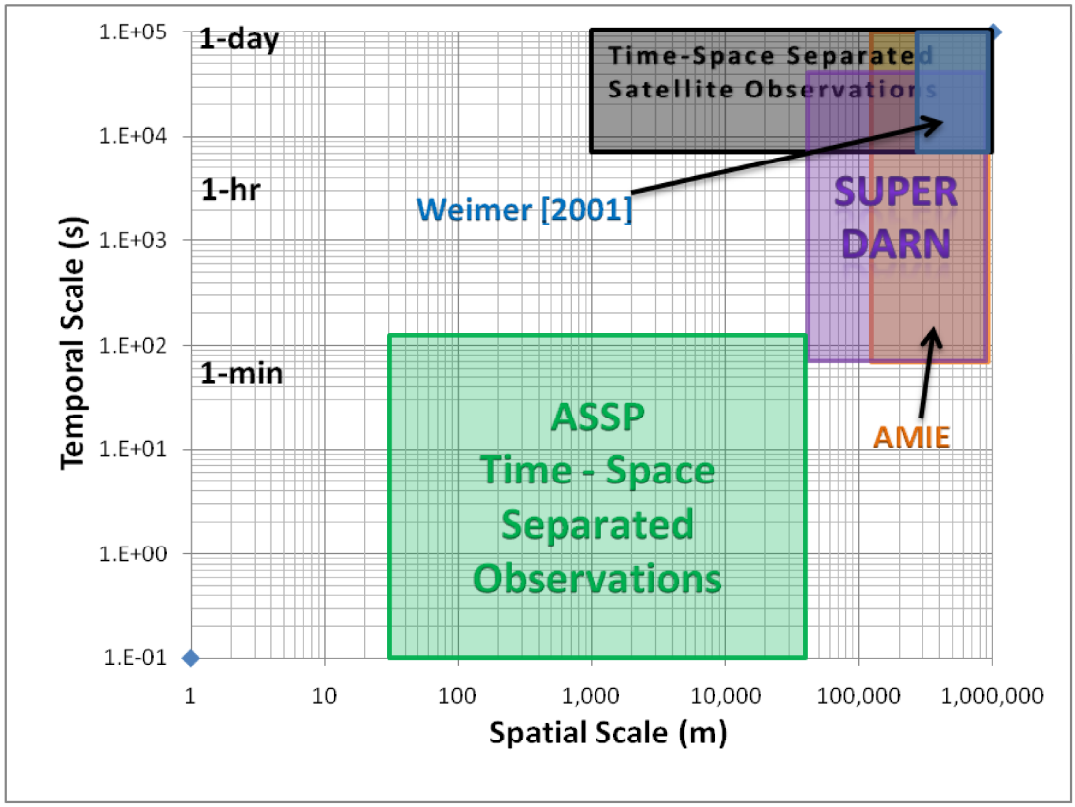

Fig. 1.2: Resolved temporal and spatial scales.

same time. After burnout, when the rocket motors have detached from the main payload and it is in free fall, it will eject six subpayloads. First, subpayloads 1 and 2 will be simultaneously ejected forwards and backwards with velocity 35 m/s relative to the main payload. A few seconds later subpayloads 3 and 4 will be simultaneously ejected forwards and backwards with velocity 17.5 m/s. Finally, subpayloads 5 and 6 will be simultaneously ejected perpendicular to the direction of motion at 35 m/s. These ejections, shown in Figure 1.3, create a cross-shaped constellation with a tip-to-tip separation up to about 60km by the end of the flight. The nominal mission timeline is reproduced in Figure 1.4.

As the ASSP constellation passes through the space environment, the location first sampled by subpayload 1 will be sampled a few seconds later by subpayload 3, then the main payload and subpayloads 4 and 2. These time separated observations make it possible to determine how the fields are changing with time in one location. Similarly, the measure-

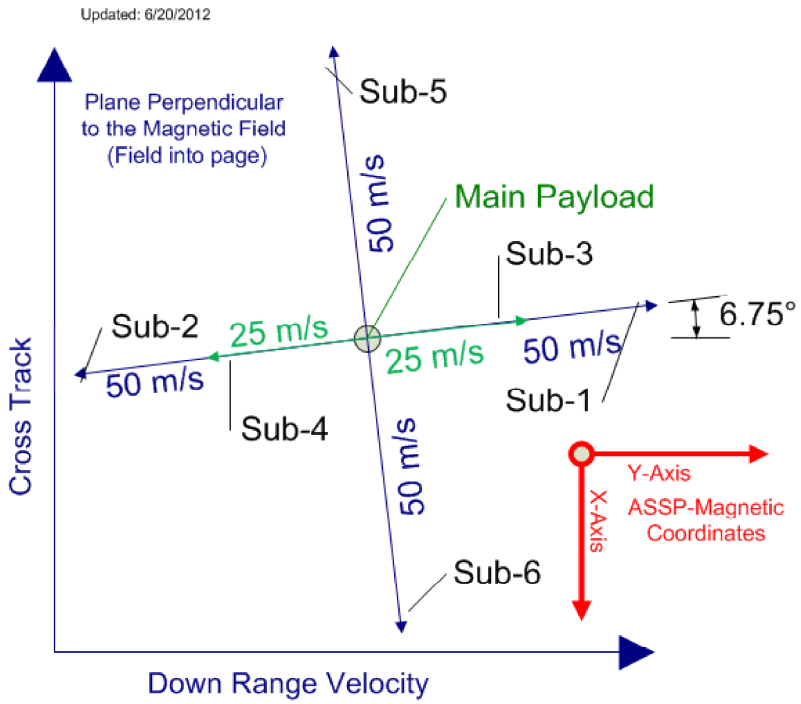

Fig. 1.3: Subpayload ejection directions.

ments taken simultaneously by all seven payloads make it possible to see how the fields are varying with location. This is how ASSP resolves the temporal spatial anomaly.

Small spatial and fast temporal measurements of the electric and magnetic fields above the aurora will allow scientists to explore how small scale fluctuations contribute to the larger scale electrodynamic processes. It will also give a clearer picture of the field-aligned currents flowing into the upper atmosphere, and help scientists to measure the relative importance of Joule versus particle heating.

1.1 Previous Missions

Only a few sounding rocket missions have attempted to achieve multipoint observation with multiple payloads. The Auroral Turbulence II sounding rocket was launched from Poker Flat, Alaska on February 11, 1997. It launched one subpayload mostly eastward and one subpayload mostly northward from the main payload at relative velocities of 10 m/s. The multipoint measurement provided by the two subpayloads enabled measurement of the proper velocity of auroral features [1, 2].

Nominal Time Line

49.002/Swenson

Weight:654 lb. CE: 83.5 deg. AZ: 8.0 deg.

3/19/2013
Rev A

Event	Time (sec)	2s Low Altitude (km)	Nominal Altitude (km)	2s High Altitude (km)	Nominal Range (km)	Nominal Q (psf)	Roll Inertia (slug-ft^2)	Main Payload Roll Rate (Hz) (after completion of event) Low	Nominal	High	Delta Sep. Velocity (ft/sec)	~Distance from main payload at 2S low 110 km downleg (km)	Event Control	Timer Type	Dwell Time	ACS maneuver time
Rail Exit	0.5	0.2	0.2	0.2	0.0	22.0							N/A	N/A	N/A	
Spin Motor Ignition	0.8	0.2	0.2	0.2	0.0	55.7							WFF Spin deck	UMFT	1	
WAASP Reset	1	0.2	0.2	0.2	0.0	86.3							main payload	UMFT	1	
Talos burnout	6.4	2.0	2.0	2.0	0.2	2345.5							N/A	N/A	N/A	
Terrier Ignition	26.0	8.1	8.1	8.2	1.3	202.0							Terrier CDI	UMFT	1	
Terrier Burnout	32.2	10.7	10.9	11.0	2.2	1630.9							N/A	N/A	N/A	
Terrier Separation	34.0	11.9	12.1	12.3	2.6	1451.1							Terrier CDI	UMFT	1	
Oriole Ignition	35.5	12.9	13.1	13.3	2.9	1165.3							Oriole CDI	UMFT	1	
Oriole Burnout	54.7	49.5	51.4	53.2	17.7	32.7							N/A	N/A	N/A	
nose cone eject	79.0	75.2	78.8	81.7	29.3	0.7						8.8	main payload	UMFT	1	
RECS deploy	81.5	79.6	83.2	86.5	31.4	0.3							LECS	pyro delay ti	N/A	
Oriole Separation	86.0	87.2	91.2	95.0	35.0	0.1							Oriole CDI	UMFT	1	
Nihka Ignition	87.0	88.8	93.0	96.9	35.6	0.1							Nihka CDI	UMFT	1	
Nihka Burnout	110.0	137.6	145.1	151.9	60.4	0.0		3.00	4.00	6.00			N/A	N/A	N/A	
De-spin to 0 Hz	113.0	145.3	153.3	160.6	64.3	0.0			0.0				Nihka CDI	UMFT	1	
Payload seperation	116.0	152.9	161.4	169.3	68.2	0.0					3.9		Nihka CDI	UMFT	1	
aft skirt separation	118.0	157.9	166.8	175.0	70.8	0.0					10.4		main payload	UMFT	1	
aft boom deploy	119.0	160.4	169.5	177.8	72.1	0.0			0.00				main payload	UMFT	1	
ACS1 roll align & pitch for sub 1 & 2 deploy (fwd end down range)	120.0	162.9	172.1	180.7	73.5	0.0							ACS	electronic		
sub 1 & 2 umbi pull (re-rad OFF)	143.0	217.7	231.0	243.3	103.1	0.0							main payload	UMFT	1	
sub 1 & 2 spin-up	145.0	222.3	235.9	248.5	105.7	0.0							main payload	UMFT	6	
ACS1 complete	150.0	233.5	248.0	261.4	112.1	0.0			0.0				ACS	electronic		30
Sub 1 (fwd end) eject	151.0	235.7	250.4	263.9	113.3	0.0					184.0	29.8	main payload	UMFT	1	
Sub 2 (aft end) eject	151.0	235.7	250.4	263.9	113.3	0.0					184.0	29.8	main payload	UMFT	1	
ACS2 roll align for sub 3 & 4 deploy	152.0	237.9	252.8	266.5	114.6	0.0							ACS	electronic		
sub 3 & 4 umbi pull (re-rad OFF)	158.0	251.0	266.9	281.5	122.2	0.0							main payload	UMFT	1	
sub 3 & 4 spin-up	160.0	255.3	271.5	286.5	124.8	0.0							main payload	UMFT	6	
ACS2 complete	164.0	263.7	280.7	296.3	129.8	0.0			0.0				ACS	electronic		12
Sub 3 (fwd end) eject	165.0	265.8	282.9	298.7	131.1	0.0					82.0	14.4	main payload	UMFT	1	
Sub 4 (aft end) eject	165.0	265.8	282.9	298.7	131.1	0.0					82.0	14.4	main payload	UMFT	1	
ACS3 roll align and pitch for sub 5 & 6 deploy (fwd end -west)	186.0	267.9	285.2	301.1	132.3	0.0							ACS	electronic		
sub 5 & 6 umbi pull (re-rad OFF)	182.0	300.1	320.1	338.6	152.3	0.0							main payload	UMFT	1	
sub 5 & 6 spin-up	184.0	304.0	324.4	343.1	154.8	0.0							main payload	UMFT	6	
ACS3 complete	188.0	311.7	332.7	352.1	159.8	0.0			0.0				ACS	electronic		22
Sub 5 (fwd end) eject	189.0	313.5	334.7	354.3	161.0	0.0					164.0	27.7	main payload	UMFT	1	
Sub 6 (aft end) eject	189.0	313.5	334.7	354.3	161.0	0.0					164.0	27.7	main payload	UMFT	1	
Fwd airspring section eject	191.0	317.3	338.8	358.7	163.5	0.0					10.4		main payload	UMFT	1	
ACS4 align to B field and trim roll rate (fwd end to -B)	192.0	319.2	340.9	360.9	164.8	0.0							ACS	electronic		
ACS4 complete	213.0	356.4	381.8	404.9	190.6	0.0	3.7	0.8	0.9	1.0			ACS	electronic		21
Hinged boom deploy	214.0	358.1	383.4	406.9	191.8	0.0	5.6	0.5	0.5	0.6			main payload	UMFT	1	
ACS5 trim alignment and roll rate	218.0	364.7	390.7	414.8	196.7	0.0							ACS	electronic		
ACS5 complete	233.0	388.4	416.9	443.3	214.9	0.0	8.8	0.4	0.5	0.6			ACS	electronic		15
stray voltage cut-off	234.0	389.9	418.6	445.1	216.1	0.0							main payload	UMFT	1	
Apogee (nominal)	439.8	N/A	599.3	N/A	436.5	0.0							N/A	N/A	N/A	
110 kM downleg (2S low)	742.9	110.1	N/A	N/A	817.6	0.0							N/A	N/A	N/A	
110 kM downleg (nominal)	782.1	N/A	109.9	N/A	868.8	0.0							N/A	N/A	N/A	
300 kft downleg (nominal)	788.5	N/A	91.3	N/A	877.3	0.2							N/A	N/A	N/A	
110 kM downleg (2S high)	821.2	N/A	N/A	110.0	914.9	4316.2							N/A	N/A	N/A	
Ballistic Impact (nominal)	835.3	N/A	0.0	N/A	917.1	1122.9							N/A	N/A	N/A	

Fig. 1.4: Mission timeline.

The Enstrophy sounding rocket launched from Poker Flat on February 11, 1999. It ejected four free flying magnetometers in a diamond pattern perpendicular to the spin axis with relative velocity of about 3.5 m/s. The multipoint measurement of the magnetic field enabled $\nabla \times B$ and $\nabla \cdot B$ to be found, which enabled the mission to directly measure field-aligned currents [3].

The Cascades2 sounding rocket mission launched from Poker Flat on March 20, 2009. Two electric field subpayloads were launched forward and backward from the main, and two smaller particle-free fliers were launched to the sides. The electric field subpayloads reached a distance of about 250 m from the main by 600 seconds flight time. The mission was able to directly measure changes in plasma drift velocity, as well as other time-varying structures [4, 5].

1.2 ASSP Payload and Instrumentation

Table 1.1 summarizes the the ASSP mission's science measurement requirements, and the instrument and mission requirements derived from them. The mission plan described above and the payload instrumentation described below have been designed to meet these science requirements.

Figure 1.5 shows an ASSP subpayload. Each subpayload carries an electric field double probe, 3-axis magnetometer, and Langmuir probe. The main payload, shown in its fully-deployed state in Figure 1.6, carries the same instruments as the subpayload plus a sweeping impedance probe and multi-bias Langmuir probe.

The electric field probe is essentially a voltmeter, with the two terminals connected to conducting spheres located at the tips of a pair of wire booms, with a 4 meter tip-to-tip separation. Since the electric field is the gradient of electric potential, a measurement of the potential difference between two points can be converted directly to the component of the electric field vector in the direction of the line connecting those two points. The ASSP sub and main payloads each carry a pair of these probes at right angles to one another, allowing a 2d vector measurement of the electric field in the body x-y plane.

Table 1.1: Science objectives to measurement requirements.

Measurement Req	Instrument Req	Mission Req
1. A constellation of payloads that progresses in separation from 35 meters to 35 km over flight 2. Measurements of E-fields on the same magnetic flux tube at different times (1 - 60 s) 3. Coincident observations of E_{perp} and ∂B-Fields 4. Observations of E-fields on scales larger than 35 km. 5. Observations of thermospheric winds	**E-field** 1. $\pm$250 mV/m range 2. $\leq$ 1.0 mV/v threshold 3. DC to 50 Hz bandwidth **B-field** 1. $\pm$0.5 Gauss range 2. $\leq$ 4 nT sensitivity 3. DC to 100 Hz bandwidth **Ground Observations** 1. $\geq$ 2 Hr before and after 2. Regional convection maps (PFISR/-SuperDARN/AMIE) 3. Winds and proxy densities (all sky imagers, Fabry-Perot Spectrometer)	1. Launch from Poker Flat Research Range to $\geq$ 600 km altitude 2. Constellation size 7 payloads 3. Max subpayload $\partial V \geq$ 35 m/s. 4. Alignment at subpayload ejection $\leq$ 1 degree (1σ) 5. Constellation time synch knowledge $\leq$ 0.01 s.

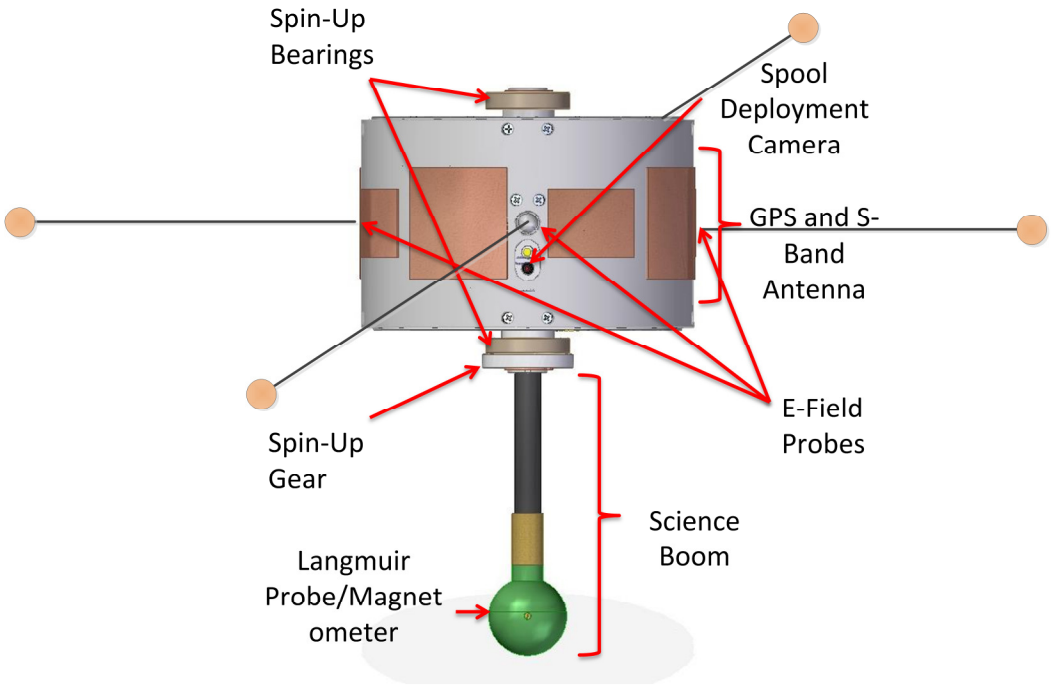

Fig. 1.5: An ASSP subpayload.

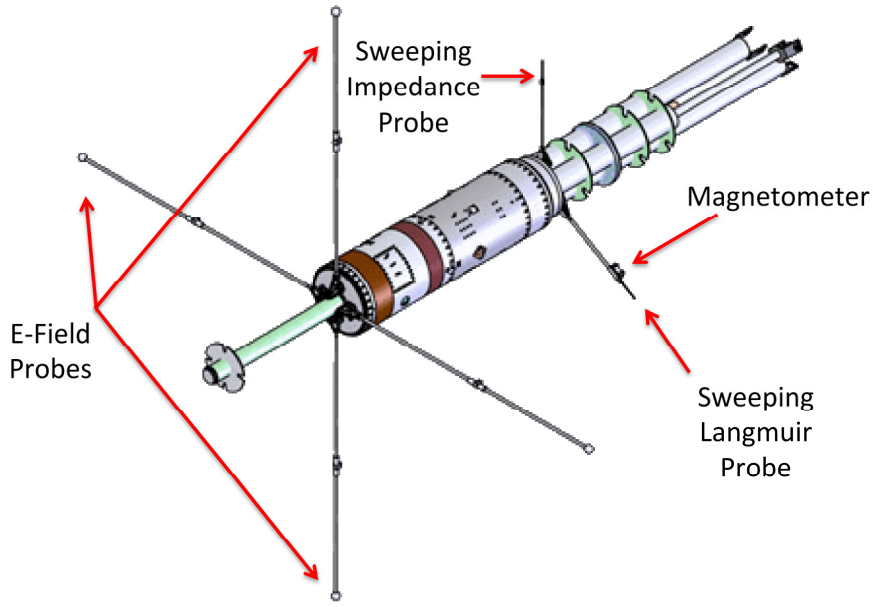

Fig. 1.6: The ASSP main payload.

The magnetometer is constructed around a magnetoresistive magnetometer manufactured by Honeywell. It is based on a Wheatstone bridge of magnetoresistive elements and outputs three voltages proportional to the magnetic field strength in the x, y, and z directions.

The Langmuir probe is a conducting sphere which is driven by payload electronics to a range of voltages relative to the space environment. The current flow to or from the Langmuir probe surface is recorded as a function of potential, and the resulting current-voltage curve can be used to find the plasma density and temperature.

Each of these instruments are continuously sampled and the data is broadcast in telemetry streams organized as shown in Figures 1.7 and 1.8. The sampling rates and word sizes shown in these charts have been chosen to meet the science requirements in Table 1.1.

The subpayloads will be ejected from the main payload by pneumatic air springs, designed and developed by NASA engineers at Wallops flight facility. Three air springs are mounted on the front of the main payload, and three on the back, with a subpayload on each spring. They can be seen in Figure 1.9, which shows the main payload in its initial

Sub Payload Telemetry Channels (AS Designed)

Channel Name	Rate Hz	Word Size bits	Wd/Samp Words	Bit Rate bits/s	Sample Period #/flight	Sample Period spatial (km)
Electric Field Probe (V12)	379	16	1	6064	227400	0.008
Electric Field Probe (V34)	379	16	1	6064	227400	0.008
EFP Wave Power (WP1 - WP16)	23.7	24	16	9101	14220	0.127
Floating Potential Probe (V1S)	379	16	1	6064	227400	0.008
Science Mag X-Axis (Bx)	379	24	1	9096	227400	0.008
Science Mag Y-Axis (By)	379	24	1	9096	227400	0.008
Science Mag Z-Axis (Bz)	379	24	1	9096	227400	0.008
Langmuir Probe (DCP-H)	379	16	1	6064	227400	0.008
Langmuir Probe (DCP-L)	379	16	1	6064	227400	0.008
Floating Potential Probe (FPP)	0.1	16	1024	1638	60	30.000
Sweeping Langmuir (SLP-H)	0.1	16	1024	1638	60	30.000
Sweeping Langmuir (SLP-L)	0.1	16	1024	1638	60	30.000
GPS		16	625	0	-	-
Spacecraft Housekeeping		16	120	0	-	-
Rate collected on orbit		Total		71624	bits/s	

Fig. 1.7: Subpayload telemetry.

Main Payload Telemetry Channels (AS Designed)

Channel Name	Rate Hz	Word Size bits	Wd/Samp Words	Bit Rate bits/s	Sample Period #/Orbit	Sample Period spatial (km)
Electric Field Probe (V12)	446.4	16	1	7142	267840	0.007
Electric Field Probe (V34)	446.4	16	1	7142	267840	0.007
EFP Wave Power (WP1 - WP16)	23.7	24	16	9101	14220	0.127
Floating Potential Probe (V1S)	0	16	1	0	-	-
Science Mag-1 X-Axis (B1x)	446.4	24	1	10714	267840	0.007
Science Mag-1 Y-Axis (B1y)	446.4	24	1	10714	267840	0.007
Science Mag-1 Z-Axis (B1z)	446.4	24	1	10714	267840	0.007
Science Mag-2 X-Axis (B2x)	446.4	24	1	10714	267840	0.007
Science Mag-2 Y-Axis (B2y)	446.4	24	1	10714	267840	0.007
Science Mag-2 Z-Axis (B2z)	446.4	24	1	10714	267840	0.007
Sweeping Langmuir (DCP-H)	0	16	1	0	-	-
Sweeping Langmuir (DCP-L)	0	16	1	0	-	-
Floating Potential Probe (FPP)	7150	16	1024	117145600	4290000	0.000
Sweeping Langmuir (SLP-H)	14300	16	1024	234291200	8580000	0.000
Sweeping Langmuir (SLP-L)	14300	16	1024	234291200	8580000	0.000
Fast Temperature (FTP1-H - FTP5-H	14300	16	5	1144000	8580000	0.000
Fast Temperature (FTP1-L - FTP5-L)	14300	16	5	1144000	8580000	0.000
Sweeping Impedance V_sin (SIP1)	20.3	24	128	62362	12180	0.148
Sweeping Impedance V_cos (SIP2)	20.3	24	128	62362	12180	0.148
Sweeping Impedance I_sin (SIP3)	20.3	24	128	62362	12180	0.148
Sweeping Impedance I_cos (SIP4)	20.3	24	128	62362	12180	0.148
GPS		16	625	0	-	-
Spacecraft Housekeeping		16	120	0	-	-
Rate collected on orbit		Total		588353114	bits/s	

Fig. 1.8: Main payload telemetry.

un-deployed state. The air springs can provide an ejection velocity of up to 35 m/s without damaging the subpayload or introducing coning or other unwanted dynamics.

Figure 1.10 shows a ground test of the air spring ejection apparatus. Figure 1.10(a) shows three subpayloads mounted on the air springs and Figure 1.10(b) shows one mass model just after ejection. The image is from a film taken by a high speed camera. In the film, no coning is visible in the mass model's motion.

1.3 Thesis Overview

This thesis focuses on two questions. The first question is: how should the ASSP constellation be created? The chosen ideal is a cross shape in which five of the payloads travel exactly the same path, but this is not realizable in free fall over the Earth. A reliable way to achieve the closest possible realizable trajectory is needed. The second question is: with what precision can ASSP measure $\vec{E}$ and $\vec{B}$? This is limited by instrument capability, but also by any uncertainty as to the position and attitude of the payloads. What is needed is an instrument testing and calibration plan, and also a coherent mathematical way to understand how the actual ASSP sensor data will be shaped by payload body dynamics.

Chapter 2 will discuss suborbital flight dynamics in the context of the goal that multiple payloads should travel the same path, and conclude that this is impossible. A "cost" function which numerically quantifies the separation between two realizable trajectories will be proposed, and an algorithm that searches for the ejection vector which minimizes this cost function will be developed. The Matlab scripts used to implement this search will be documented.

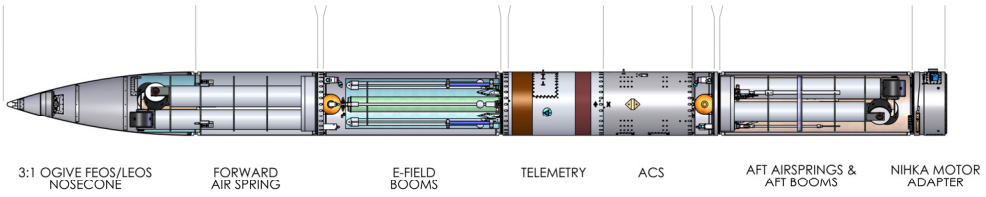

Fig. 1.9: The ASSP main payload before ejection and boom deployment.

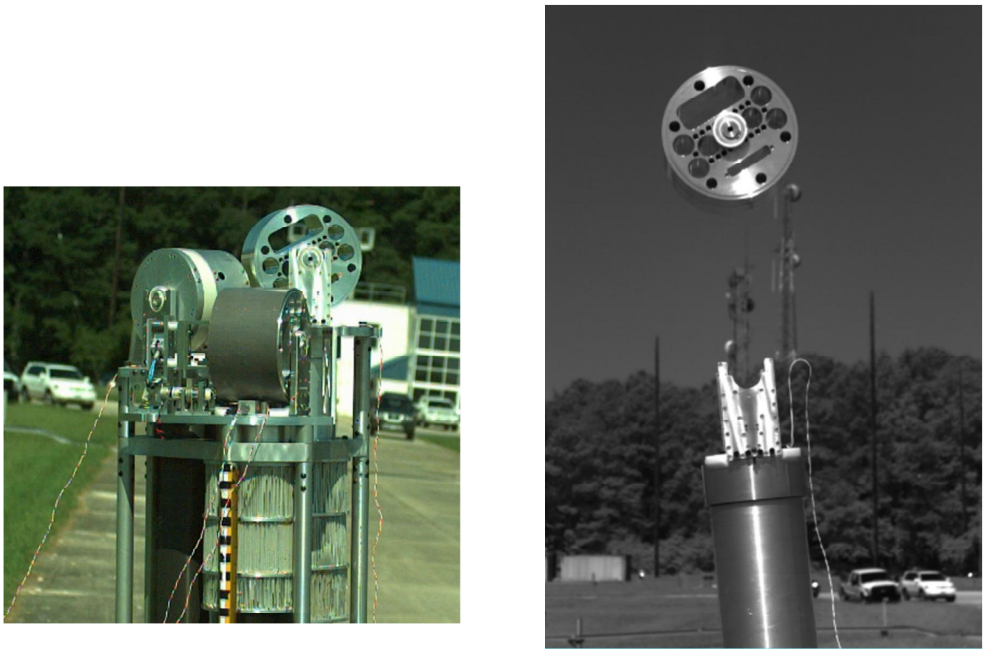

(a) ASSP subpayloads mounted on the ejection apparatus.

(b) Ejection test.

Fig. 1.10: Ejection hardware testing.

Chapter 3 will develop forward and inverse mathematical models of the ASSP science instruments, and discuss how these can be used for calibration purposes.

Chapter 4 will describe the tests that must be performed in order to calibrate the ASSP science instruments, and propose a method for automating the testing process as much as possible. The design of the custom hardware which must be built to support the automated test plan will be described.

The Appendix describes the contents of an archival DVD to be kept with copies of the printed thesis, which contains all the files, documents, and source code pertaining to this thesis.

Chapter 2

Ejection Angle Optimization

2.1 Objective

In order for the ASSP mission to accomplish its science goals, multiple payloads must successively pass through and sample the same magnetic flux tube. The orientation of the main payload when the subpayloads are ejected is the only parameter available to control the trajectories of the subpayloads. It is therefore necessary to identify the ejection vectors which will cause payloads 1, 2, 3, 4, and main to share the smallest possible magnetic flux tube. This chapter will explore, define, and solve the problem of identifying these ejection vectors.

2.1.1 Motion in a Non-Inertial Frame of Reference

In an inertial reference frame, it is easy to make two objects with different velocities trace the same path: simply launch them in the same direction. In a rotating frame of reference, however, the situation is very different. The ordinary laws of motion in an inertial frame of reference can be used to describe motion in a non-inertial reference frame if three fictitious forces are considered to act on a moving body, in addition to any actual forces. Newton's second law,

$$\vec{F} = m\vec{a}, \tag{2.1}$$

becomes

$$\vec{F} - m\dot{\vec{\omega}} \times \vec{r} - m\vec{\omega} \times (\vec{\omega} \times \vec{r}) - 2m\vec{\omega} \times \vec{v} = m\vec{a}, \tag{2.2}$$

where $\vec{\omega}$ represents the angular velocity of the reference frame.

An observer on Earth will see objects obeying Equation (2.2) rather than Equation (2.1). Since the magnetic structures to be sampled are fixed to the Earth, it is worth-

while to examine the extra terms in Equation (2.2) and get a sense for what effect they will have on a ballistic trajectory. In particular, note the Coriolis term, $2m\vec{\omega}\times\vec{v}$. It is perpendicular to the direction of motion and its magnitude is proportional to velocity. Therefore, the path of a fast-moving object will curve to the left or the right and, importantly, the sharpness of the curvature will be a function of its velocity. Two objects traveling at different velocities cannot share the same trajectory.

The problem of subpayload ejection is thus an optimization problem. Any chosen ejection vector will result in a subpayload trajectory that differs to a greater or lesser degree from the main payload trajectory. This difference should be expressed as a numerical "cost," and then the ejection vector with the minimum cost should be identified.

2.1.2 The Parameter to be Optimized

As previously said, multiple payloads should ideally pass through the same magnetic flux tube. A magnetic flux tube is a structure defined such that the local magnetic field at its surface is always parallel to that surface. The cross sectional shape and area of a tube may change along its length, but the enclosed magnetic flux is a constant. Since magnetic flux tubes are an abstract structure, it is always possible to construct one wide enough that any two payloads will sample it. However, the size of the flux tube being sampled influences the minimum size of the spatial scales that can be examined. It is desirable to repeatedly sample the smallest flux tubes possible. This means that the separation between two trajectories, which is the cost to be minimized, is not the ordinary physical distance between the payloads but the size of the magnetic flux tube they share. Figure 2.1 depicts two payloads passing through the same magnetic flux tube at different altitudes. The altitude difference between the two payloads is very small compared to the scales over which the perpendicular electric fields are changing.

Note that spatial distances along the magnetic field lines do not contribute to separation as defined above. Two points on the same field line have no separation between them, no matter how spatially distant they may be. This enables the problem to be converted from 3d to 2d, by projecting payload positions to a sphere of constant altitude *along the magnetic*

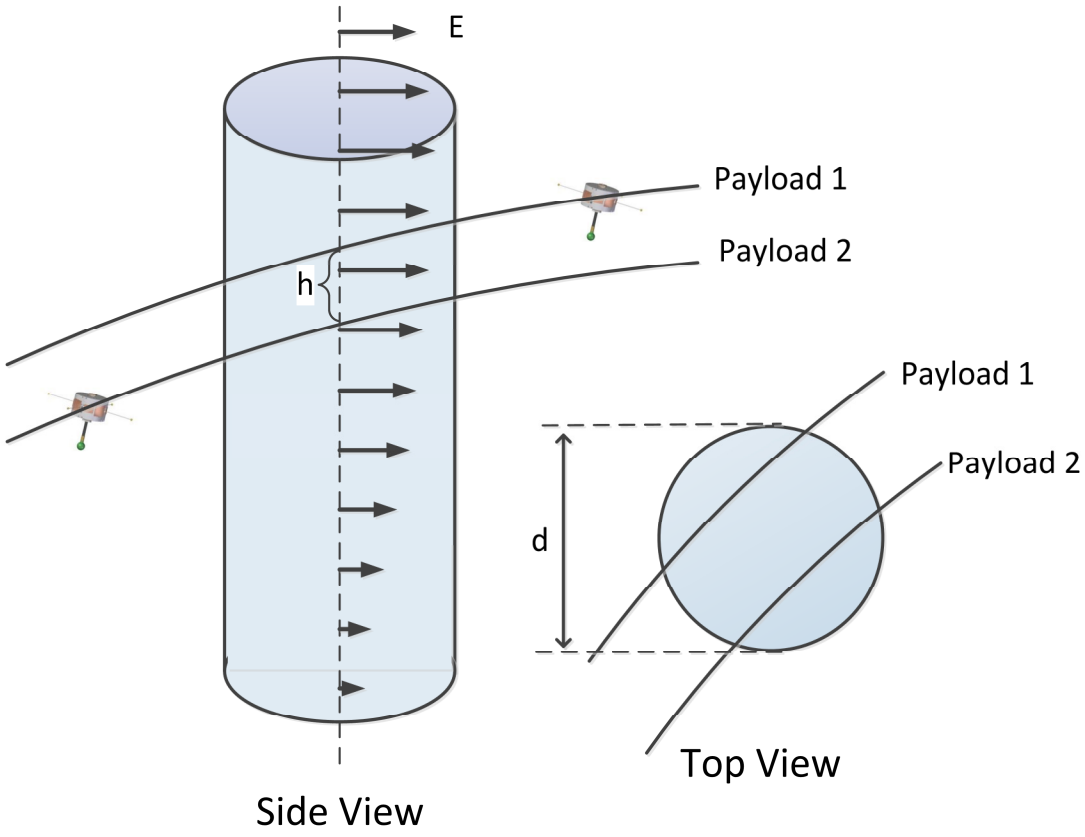

Fig. 2.1: Two payloads passing through the same flux tube.

field lines. In this 2d representation of a 3d space, the separation between two points is simply the great-circle distance between them.

With separation between two points clearly defined, it becomes possible to define separation between two curves. The total area between the curves would be a valid metric to use, but it is not simple to compute for curves that are defined as a series of discrete points. The proposed metric is a sum, over every point on curve 1, of the distance to the nearest point on curve 2. Figure 2.3 is a cartoon depiction of the "groundtracks" of the main payload and a subpayload. On one of the points on the right-hand groundtrack, the distances to the two nearest points on the other groundtrack are highlighted with dashed lines. The cross section of the smallest magnetic flux tube shared by the two tracks at this point is represented as a circle. If the distance between two neighboring points along one groundtrack is small compared to the distance between the two groundtracks, the shorter of the dashed lines would be a good approximation of the diameter of the circle. But because of computation time constraints, the distance between points on one groundtrack is significantly greater than the distance between the two tracks.

This difficulty was resolved by using spline interpolation to greatly increase the number of points on each curve. Because the groundtracks are smooth and lack discontinuities, interpolation will not distort them. However, the greatly increased number of points caused a new problem: searching curve 2 for the point nearest to each point on curve 1 now takes too much time. This speed penalty was mitigated by measuring the distance between the two curves where they have the same latitude, rather than where they are closest. Testing has shown that this approximation identifies the same ejection angle as the more time consuming technique.

It is worth noting that the sum of distances described above could be normalized to an approximation of the area between the curves by multiplying it by the distance from point to point along curve 1. However, there is no compelling need to do this, since this value is to be used as a cost function to be minimized. The absolute magnitude of the value is unimportant.

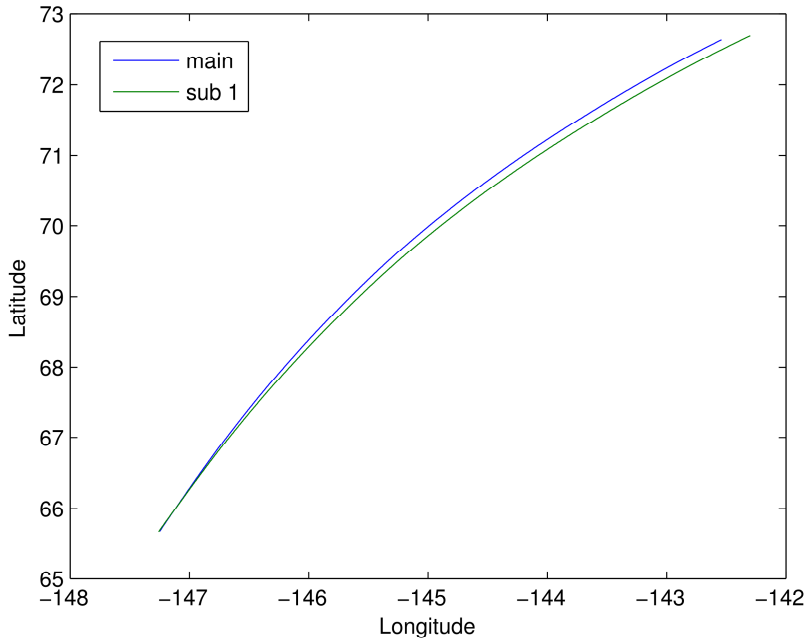

Fig. 2.2: Main and subpayload 1 trajectories projected to a common altitude.

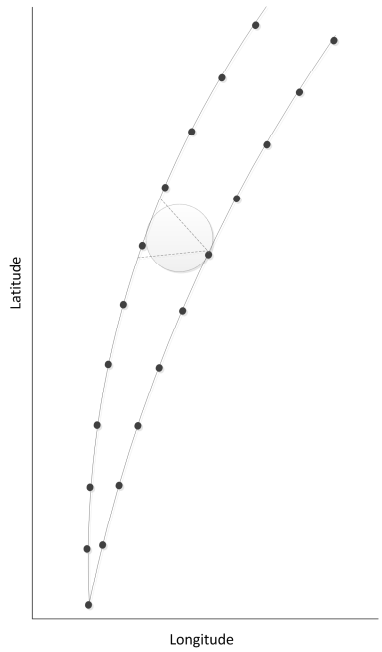

Fig. 2.3: Main and subpayload 1 trajectories with exaggerated point-to-point separation.

2.2 Implementation

The Matlab scripts that provide the ASSP ejection target perform the following tasks:

1. Numerically simulate the post-burnout trajectory of the main payload;
2. Define a range of possible ejection vectors for the subpayload under consideration;
3. Numerically simulate the post-ejection trajectory of the subpayload for each possible ejection vector;
4. Calculate the cost of each subpayload trajectory, as defined in section 2.1;
5. Save the ejection vector corresponding to the minimum cost.

This procedure must be repeated for each subpayload, and for a range of possible main payload trajectories

2.2.1 Main Payload Dispersion

Since the ASSP sounding rocket will be unguided during the burn stage of flight, the range of possible main vehicle trajectories is very great. Figure 2.4, which was produced by engineers at NASA Wallops, shows authorized impact areas and possible impact ranges for the first and last engine stages. What is especially relevant here is the impact range of the final stage and therefore main payload, shown by the three large circles in the Arctic Ocean which represent the 1σ, 2σ, and 3σ dispersion areas. These ranges were found by a Monte-Carlo simulation: the rocket flight was simulated with realistic random variation in performance 1001 times. Six hundred and eighty of the virtual rockets landed within the first circle, 950 of them landed within the second, and so on.

The Monte-Carlo simulation was also used to provide the set of main payload trajectories for the ejection optimization algorithm to act on. The Matlab scripts take as input a table of 1001 state vectors at time $t = 116$ seconds. These state vectors are after burnout when the payload is in free fall, so it is straightforward to simulate the full post-burnout

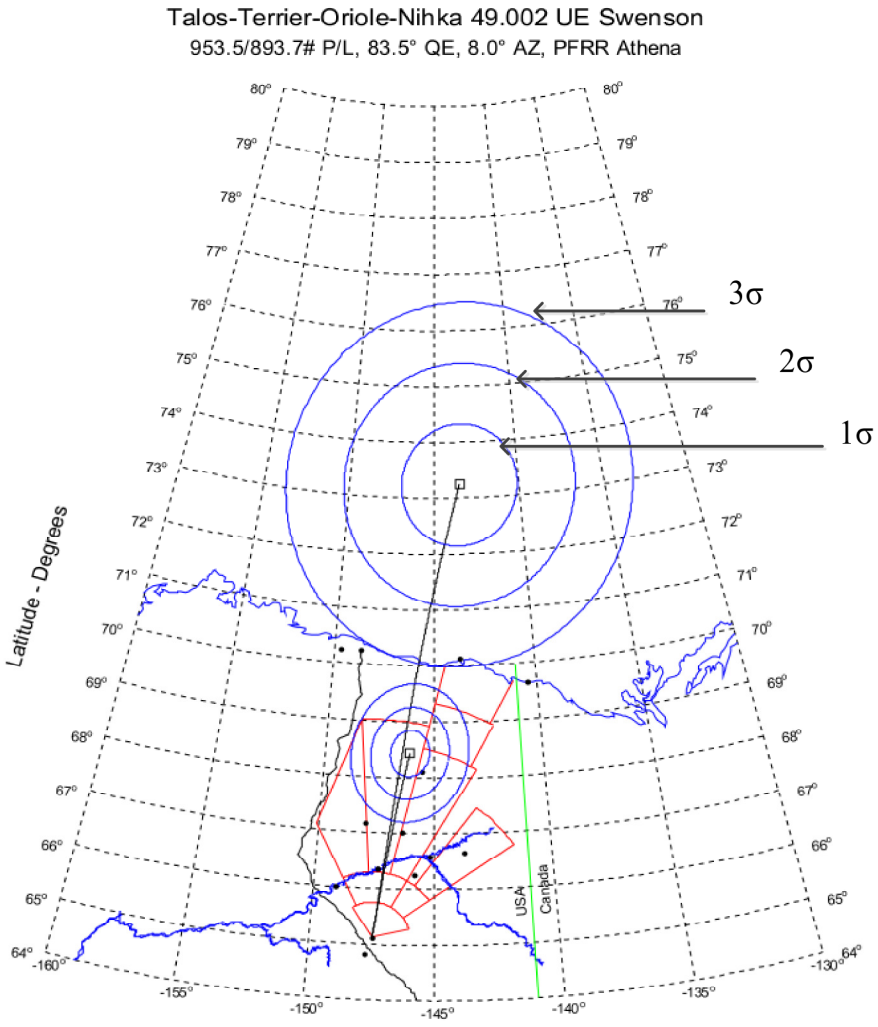

Figure 3.5-2 Nihka Impact

Fig. 2.4: Map showing 1, 2, and 3σ main payload impact range (courtesy of NASA).

trajectory. The optimal ejection vector for each trajectory is identified and saved, resulting in a table of 1001 state vectors with corresponding unit vectors in the direction of the optimal ejection.

2.2.2 Architecture

Figure 2.5 shows the files used to produce a table of optimal ejection vectors. All of the Matlab scripts were developed as part of this thesis work. The executable MagTrace2.exe was provided by Mike Disbrow at Wallops flight facility. This section contains a brief high-level overview of what the most important functions do.

The function gtof.m takes a state vector at $t = 116$ seconds as input and returns a unit vector in the direction of the optimal ejection. It simulates the full trajectory of the main payload, and then chooses an ejection angle and creates a post-ejection state vector for the subpayload by adding an ejection velocity vector to the main payload state vector at time of ejection. The velocity vectors considered are those in the plane perpendicular to the expected $\vec{B}$ at apogee, and different from the projection of the main payload velocity into said plane by the ejection angle. The subpayload state vector is passed to subtrack.m, which returns a full trajectory for the subpayload. The main and subpayload trajectories are passed on to gtsplinefit.m, which returns the cost of the trajectories. gtof.m repeats this procedure for many ejection angles, and returns the angle and corresponding unit vector with the minimum cost.

The function gtsplinefit.m finds the cost associated with a pair of trajectories by first passing them to passtomagtrace.m, which returns the trajectories projected along the magnetic field lines to an altitude of 120 km. Both trajectories are then spline interpolated, which dramatically increases the number of points on the curve. Finally, the function sums, over each latitude, the longitudinal distance between the curves.

2.2.3 ACS Pointing Objective

The output of the program defined above is a table of 1001 unit vectors in the direction of the optimal ejection (referred to hereafter as ejection vectors), each corresponding to a

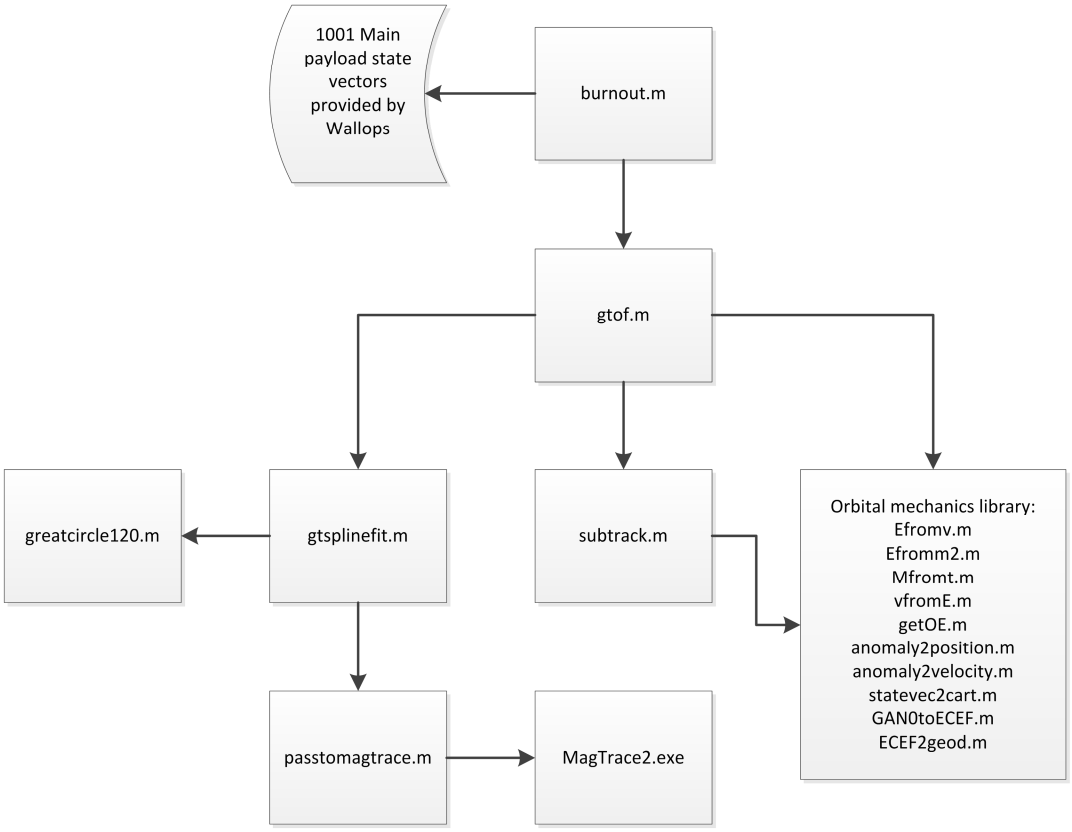

Fig. 2.5: Matlab script dependency flowchart.

main payload state vector at $t = 116$ seconds. This is not a convenient way to provide the ASSP ADCS with orientation targets. The ADCS needs to be able to quickly compute the optimal ejection vector for the actual trajectory it happens to be flying based on parameters it has access to. Using the $t = 116$ s state vector as the input is good, since the ADCS will have access to that information several seconds before it must start to orient itself for ejection. However, the actual $t = 116$ s state vector will not be identical to any of the state vectors in the simulated table, and interpolating in six dimensions is too complex to attempt in real time.

The used solution is to create a multivariable polynomial regression model of the table. Each component of the ejection vector is represented as a polynomial in the six components of the $t = 116$ s main payload state vector. What should the form of the polynomial be? There is no obvious way to predict ahead of time what functional form would make sense. The terms used were identified using the stepwise regression algorithms included in the Matlab Statistics Toolbox. A model with many terms was chosen to start, and statistically insignificant terms were removed one by one. The final form of the function is

$$\begin{aligned} e_i = {} & b_0 + b_1 x + b_2 y + b_3 z + b_4 \dot{x} + b_5 \dot{y} + b_6 \dot{z} + b_7 x\dot{x} + b_8 y\dot{x} \\ & + b_9 \dot{x}^2 + b_{10} y\dot{y} + b_{11} \dot{x}\dot{y} + b_{12} \dot{y}^2 + b_{13} \dot{x}\dot{z} + b_{14} \dot{y}\dot{z} + b_{15} \dot{z}^2 \\ & + b_{16} x\dot{x}^2 + b_{17} y\dot{x}\dot{y} + b_{18} \dot{x}^2\dot{y} + b_{19} \dot{x}\dot{y}^2 + b_{20} \dot{x}^2\dot{z} + b_{21} \dot{x}\dot{y}\dot{z} \\ & + b_{22} \dot{y}^2\dot{z} + b_{23} \dot{x}\dot{z}^2 + b_{24} \dot{y}\dot{z}^2. \end{aligned} \tag{2.3}$$

The coefficients for subpayload 1 are summarized in Figure 2.6. All coefficients for all ejections have been stored on disc and sent to the ADCS engineers at Wallops. The polynomial approximation adds very little error. Figure 2.7 is a scatter plot of the simulated and polynomial approximated value of e_z for subpayload 5. Aside from two or three (out of a thousand!) outliers, every point lies along the $x = y$ line. The "fuzzing" of the line is due mostly to the discrete nature of the simulated output versus the continuous polynomial output.

Sub 1

x	value
b0	0
b1	-4.73E-08
b2	3.60E-07
b3	2.10E-07
b4	-0.0094553
b5	-0.0023781
b6	-0.0001812
b7	-1.48E-09
b8	-4.29E-10
b9	6.69E-06
b10	1.53E-10
b11	2.21E-06
b12	-3.18E-06
b13	3.93E-06
b14	8.30E-07
b15	3.42E-08
b16	2.84E-12
b17	4.81E-13
b18	-2.68E-10
b19	-4.59E-11
b20	-1.91E-10
b21	-3.14E-10
b22	1.03E-09
b23	-6.50E-10
b24	-4.52E-11

y	value
b0	0
b1	2.03E-07
b2	1.97E-07
b3	-6.71E-07
b4	0.017072
b5	-0.00984
b6	0.00354
b7	1.99E-10
b8	-8.45E-10
b9	-4.32E-06
b10	2.21E-09
b11	-6.48E-06
b12	1.92E-07
b13	-1.18E-05
b14	9.29E-06
b15	-5.82E-07
b16	-1.07E-12
b17	-5.05E-12
b18	-1.59E-10
b19	8.99E-10
b20	7.11E-10
b21	-2.32E-10
b22	-2.80E-10
b23	1.90E-09
b24	-1.59E-09

z	value
b0	0
b1	3.35E-08
b2	2.39E-07
b3	-8.35E-08
b4	2.83E-05
b5	-0.00399
b6	0.00091
b7	-6.98E-10
b8	-4.57E-10
b9	2.18E-06
b10	7.03E-10
b11	-7.10E-07
b12	-1.56E-06
b13	-1.35E-06
b14	3.05E-06
b15	-1.47E-07
b16	1.14E-12
b17	-1.19E-12
b18	-1.81E-10
b19	2.31E-10
b20	1.04E-10
b21	-2.25E-10
b22	4.44E-10
b23	2.06E-10
b24	-4.74E-10

theta	value
b0	0
b1	2.28E-07
b2	1.30E-07
b3	-6.43E-07
b4	0.019452
b5	-0.00844
b6	0.003147
b7	2.72E-10
b8	-6.95E-10
b9	-5.29E-06
b10	1.83E-09
b11	-4.16E-06
b12	-1.83E-07
b13	-1.29E-05
b14	7.38E-06
b15	-5.16E-07
b16	-1.35E-12
b17	-4.07E-12
b18	-1.15E-10
b19	6.43E-10
b20	8.13E-10
b21	-5.32E-10
b22	-7.50E-11
b23	2.06E-09
b24	-1.22E-09

Fig. 2.6: Subpayload 1 polynomial coefficients.

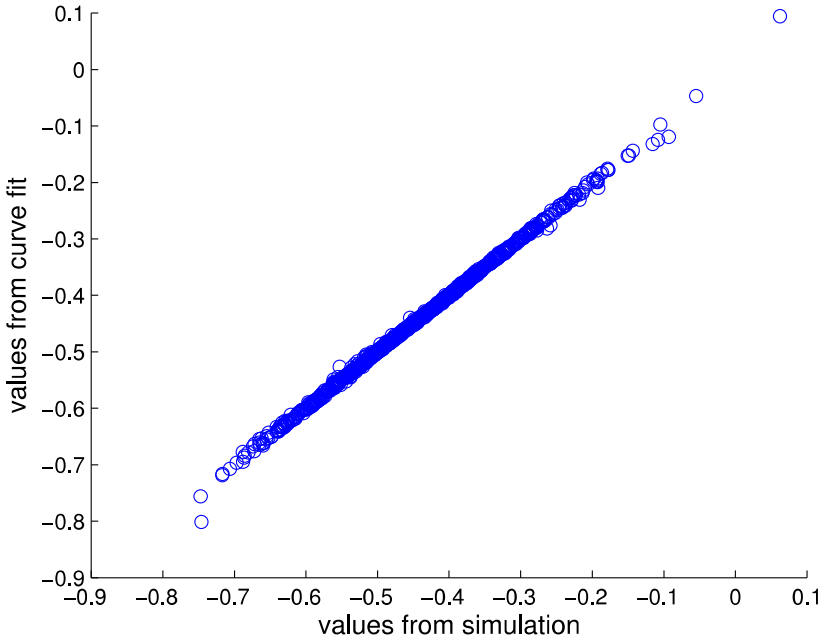

Fig. 2.7: Actual target versus polynomial approximation.

2.3 Results

This chapter has talked at length about optimizing the separation between trajectories, but how optimal is the optimum solution? Figure 2.8 shows the separation between the main payload and the nearest point on subpayload 1's trajectory as a function of time. It is plotted both as an absolute crosstrack separation distance and as a relative distance, which is the crosstrack separation divided by the total downrange distance between the payloads at that time. The relative separation stays well below 1%, showing that in terms of the spatial scale the mission is sampling, the separation is very small indeed. Figure 2.9 shows the crosstrack separation between the main payload and each subpayload as a function of time.

Of course, the above discussion assumes that the ADCS is able to eject the subpayloads at the exact angle requested by the algorithm. In reality, the 2σ ADCS pointing error is expected to be about 1 degree. Figure 2.10 shows the consequences of pointing 1 degree to the left or right. Things certainly look worse, but not catastrophically so. Even if the ejection angle is off by 2σ the separation will be more than small enough to satisfy the mission science requirements.

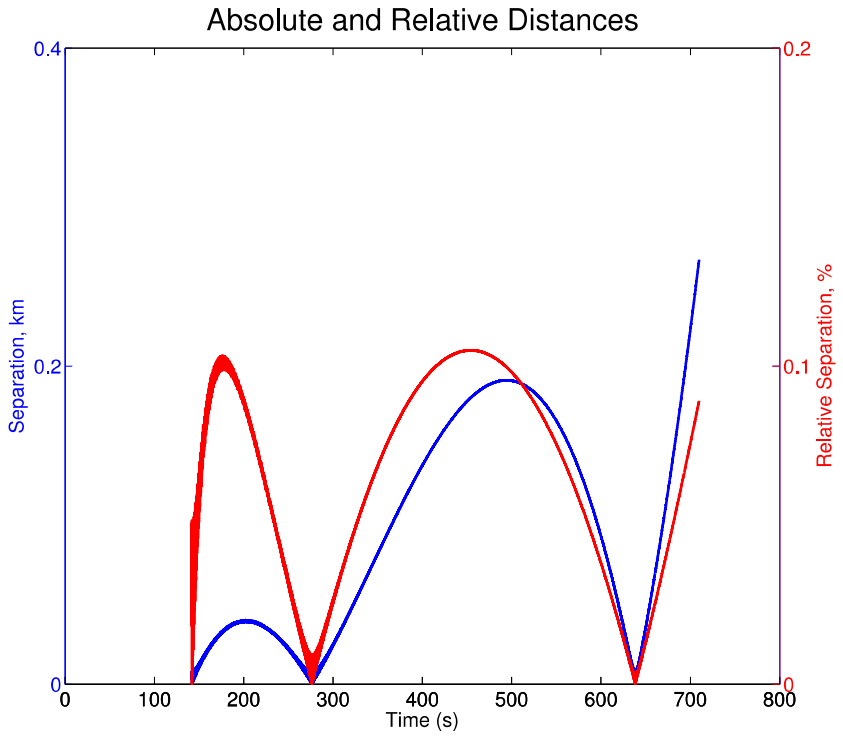

Fig. 2.8: Crosstrack separation between the main payload and subpayload 1.

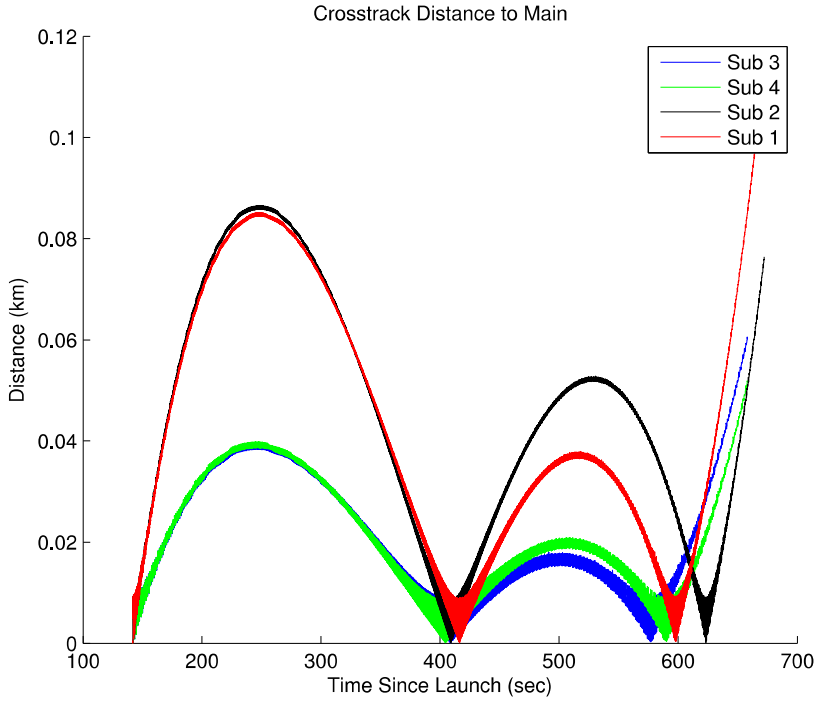

Fig. 2.9: Crosstrack separation between the main payload and each subpayload.

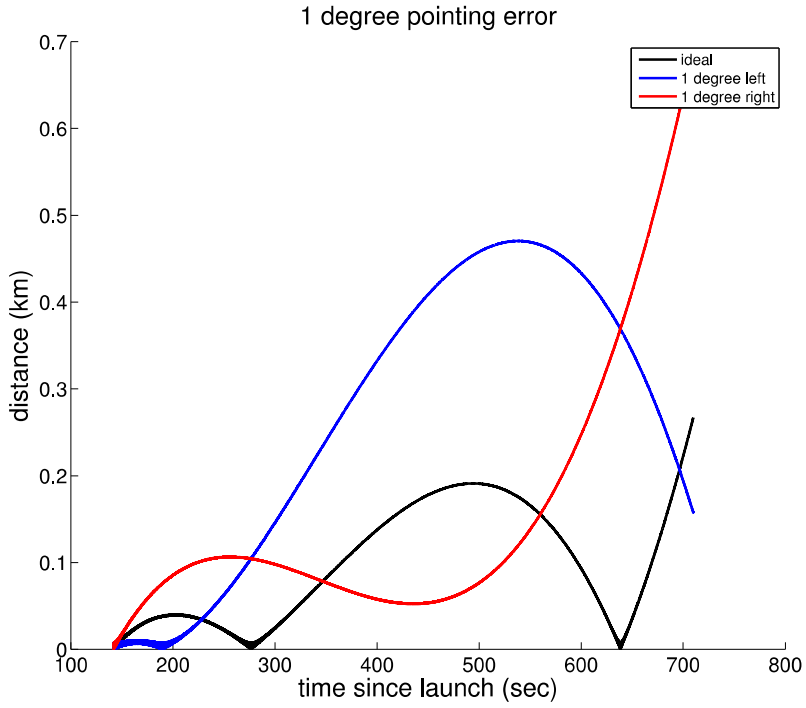

Fig. 2.10: Consequences of error in ejection angle.

Chapter 3

Instrument Calibration Theory

The ASSP science instruments record the measurements they make as pulse-code modulation (PCM) counts, integer values which are transmitted over the telemetry stream. For these values to be of any scientific use, there must be a calibration model, a mathematical function with instrument PCM count as input and a physical value as output. This chapter will examine each instrument's electronics, derive a mathematical transfer function that models the physical means by which the instrument converts its input to a PCM count, and find the inverse of said transfer function.

3.1 Electric Field Probe

The ASSP electric field probe senses the electric potential between two conducting spheres with an INA116 instrumentation amplifier. Figure 3.1 depicts the system. Both inputs to the INA116 are shielded by driven guards, which suppress the amplifier's effective input capacitance.

The voltage at the amplifier input is

$$V_m = \frac{R_i}{R_S + R_i} V_S. \tag{3.1}$$

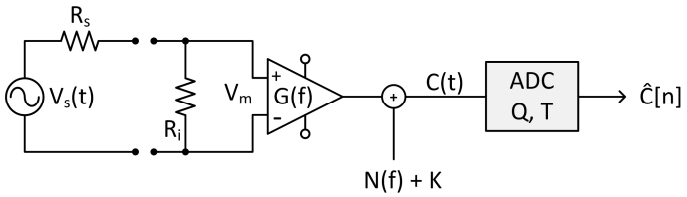

Fig. 3.1: Model of the E-field instrument.

The resistance of the space plasma environment is large, so the INA116 was chosen for its very large input resistance (10^{15} Ω) in order to make V_m as close to V_S as possible. The voltage sources that will be used for ground testing have much much smaller output resistances, so for test events V_m will be assumed equal to V_S.

The amplifier has a transfer function $G(f)$ which will be measured experimentally, with the assumption that

$$G(f) = |H(j2\pi f)|, \tag{3.2}$$

which is true if the transfer function $H(j\omega)$ has linear phase. The ASSP electronics have been designed such that all filters have this characteristic.

For a sinusoidal input,

$$V_S(t) = A\cos(2\pi f t), \tag{3.3}$$

and neglecting the system noise $N(f)$, the signal at the the analog-to-digital converter will be

$$C(t) = A\cos(2\pi f t)G(f) + K, \tag{3.4}$$

where $G(f)$ is the gain of the amplifier at the frequency f. The analog to digital converter samples and quantizes the continuous time-varying variable $C(t)$ into the discrete quantized variable $\hat{C}[n]$. The relationship between the two quantities is

$$Q\hat{C}[n] = C(nT), \tag{3.5}$$

where T is the sampling period and Q is the quantization interval or step size.

Equation (3.4) can be rewritten for $\hat{C}$ as

$$\hat{C}[n] = A\cos(2\pi f n T)G(f)/Q + K/Q. \tag{3.6}$$

By comparing Equation (3.6) with the corresponding input in Equation (3.3), it can be seen that the functional relationship between $\hat{C}$ and V_S takes the form

$$\hat{C} = A(f)V_S + B, \tag{3.7}$$

where A and B are fit parameters to be determined experimentally, and A will depend on the input frequency. The inverse model is

$$V_S = \frac{\hat{C} - B}{A(f)}. \tag{3.8}$$

Although the discussion above leads one to expect that a linear model is appropriate for the E-field instrument, it makes sense to also try fitting a 2nd order polynomial model to see if it better accounts for realities not represented in the simplified picture of the system. This would take the form

$$\hat{C} = A(f)V_S^2 + B(f)V_S + C, \tag{3.9}$$

the inverse of which is

$$V_S = \frac{-B(f) \pm \sqrt{(B(f))^2 - 4A(f)(C - \hat{C})}}{2A(f)}. \tag{3.10}$$

3.2 Magnetometer

The ASSP magnetometer is a 3-axis instrument, but this discussion will for simplicity treat only a single axis. Magnetic fields are sensed by four magnetoresistive elements in a Wheatstone bridge configuration, shown in Figure 3.2. Two of the bridge elements increase in resistance as the applied field increases, and two decrease.

For a sinusoidal magnetic field,

$$B_x(t) = A\cos(2\pi f t), \tag{3.11}$$

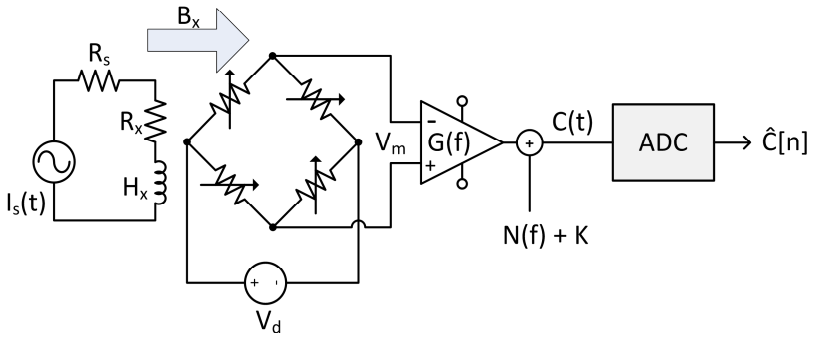

Fig. 3.2: Model of the magnetometer.

the potential seen at the input to the amplifier will be

$$V_m(t) = \frac{-SB_x(t)}{2R} V_d = \frac{-SV_d}{2R} A\cos(2\pi f t), \tag{3.12}$$

where R is the nominal resistance of the bridge elements and S is the rate at which resistance changes due to applied field, which should be a constant over the range of magnetic fields the device will be exposed to. The signal at the the analog-to-digital converter will be

$$C_x(t) = \frac{-SB_x(t)}{2R} V_d G(f) + K_x = \frac{-SV_d G(f)}{2R} A\cos(2\pi f t) + k_x, \tag{3.13}$$

However, since R, S, and V_d are all constants, the term $\frac{-SV_d G(f)}{2R}$ can be collapsed into one term, so that Equation (3.13) becomes

$$C_x(t) = m_x(f) A\cos(2\pi f t) + K_x. \tag{3.14}$$

Equation (3.14) can be rewritten in terms of $\hat{C_x}$ as

$$\hat{C_x}[n] = m_x(f) A/Q\cos(2\pi f n T) + K_x/Q. \tag{3.15}$$

As was the case for the electric field probe, the functional relationship between B_x and $\hat{C}_x$ is linear:

$$\hat{C}_x = A(f)B_x + B, \tag{3.16}$$

where A and B are fit parameters to be determined experimentally, and A will depend on the input frequency. The inverse model is

$$B_x = \frac{\hat{C}_x - B}{A(f)}. \tag{3.17}$$

As in the previous section, although the discussion above leads one to expect that a linear model is appropriate for the magnetometer, it makes sense to also try fitting a 2nd order polynomial model to see if it better accounts for realities not represented in the simplified picture of the system. This would take the form

$$\hat{C}_x = A(f)B_x^2 + B(f)B_x + C, \tag{3.18}$$

the inverse of which is

$$B_x = \frac{-B(f) \pm \sqrt{(B(f))^2 - 4A(f)(C - \hat{C}_x)}}{2A(f)}. \tag{3.19}$$

The above discussion could be repeated for the y and z axes, which would completely characterize the magnetometer if all three sensitive axes were perfectly geometrically aligned. An applied field purely in the y direction would affect only $\hat{C}_y$. In reality, the magnetometer axes may not be perfectly orthogonal to one another, and the magnetometer itself may not be precisely aligned with the spacecraft body axes in which the measurement is considered to be taken. This will result in cross contamination: an applied field purely in the y direction will produce a response in $\hat{C}_y$, but also smaller responses in $\hat{C}_x$ and $\hat{C}_z$.

The cross contamination can be accounted for by replacing the scalar fit parameter $A(f)$ in Equation (3.16) with a 3×3 matrix A, yielding:

$$\begin{bmatrix} \hat{C}_x \\ \hat{C}_y \\ \hat{C}_z \end{bmatrix} = \mathsf{A} \cdot \begin{bmatrix} B_x \\ B_y \\ B_z \end{bmatrix} + \vec{b}, \tag{3.20}$$

or more explicitly

$$\begin{bmatrix} \hat{C}_x \\ \hat{C}_y \\ \hat{C}_z \end{bmatrix} = \begin{bmatrix} a_{1,1} & a_{1,2} & a_{1,3} \\ a_{2,1} & a_{2,2} & a_{2,3} \\ a_{3,1} & a_{3,2} & a_{3,3} \end{bmatrix} \cdot \begin{bmatrix} B_x \\ B_y \\ B_z \end{bmatrix} + \begin{bmatrix} b_1 \\ b_2 \\ b_2 \end{bmatrix}. \tag{3.21}$$

The twelve fit parameters in the above equation can be determined experimentally. The inverse model is

$$\begin{bmatrix} B_x \\ B_y \\ B_z \end{bmatrix} = \mathsf{A}^{-1} \cdot \begin{bmatrix} \hat{C}_x - b_1 \\ \hat{C}_y - b_2 \\ \hat{C}_z - b_3 \end{bmatrix}, \tag{3.22}$$

where A^{-1} is the matrix inverse of A. Note that if the axes are perfectly aligned and there is no cross contamination, A is diagonal and Equation (3.21) reduces to three independant equations of the same form as Equation (3.16).

3.3 Trimming the Magnetometer

Figure 3.3 shows how the three magnetometer bridges are electrically connected. Ideally, when no magnetic field is applied the bridges are balanced, meaning that—to pick the X bridge arbitrarily—$\frac{R_1}{R_2}$ is exactly equal to $\frac{R_3}{R_4}$, and therefore $X+ = X-$. In reality there are always small variations in the resistance of individual elements, which means there will be some offset in the output voltage. Of course, voltage offset is accounted for in the calibration model presented above, but if the offset voltage is significant compared to the linear range of the device, then much of the useful range is wasted. Therefore, it is worthwhile to physically intervene to reduce the actual offset as much as possible.

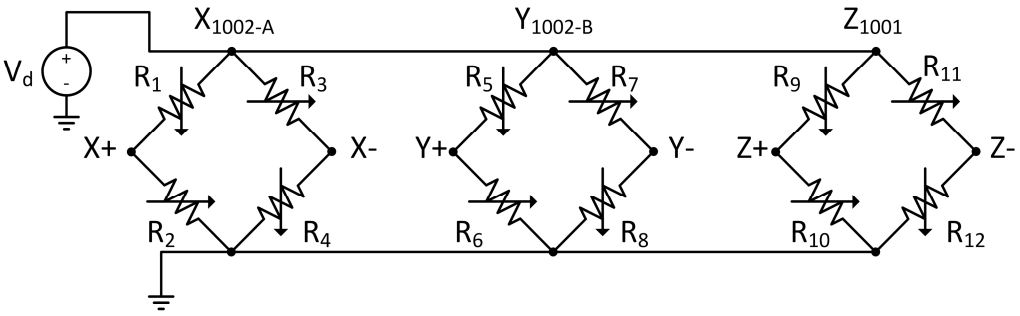

Fig. 3.3: The three magnetometer bridges.

A bridge can be balanced by adding a comparatively large external resistor R_T in parallel with one of the internal resistive elements. The effective resistance of that element will then be its own resistance in parallel with that of R_T. If the true resistance of each bridge element is known it is straightforward to calculate the magnitude of R_T that will balance the bridge. For example, if $\frac{R_1}{R_2} > \frac{R_3}{R_4}$, then either R_1 or R_4 should be reduced to balance the bridge. If R_1 is chosen then the R_T which will balance the bridge can be found by solving the equation

$$\frac{R_1||R_T}{R_2} = \frac{R_3}{R_4}. \tag{3.23}$$

Unfortunately, measuring the resistance of each element is nontrivial, since the connections depicted in Figure 3.3 cannot be removed. An Ohm meter connected to nodes $X+$ and ground will not measure R_2 but $R_2||(R_1 + R_3 + R_4)$. In theory one can make measurements like this and then solve the system of equations

$$R_{M1} = R_1||(R_2 + R_3 + R_4) \tag{3.24}$$

$$R_{M2} = R_2||(R_1 + R_3 + R_4) \tag{3.25}$$

$$R_{M3} = R_3||(R_1 + R_2 + R_4) \tag{3.26}$$

$$R_{M4} = R_4||(R_1 + R_2 + R_3) \tag{3.27}$$

for R_1, R_2, R_3, and R_4. However, when this was done the resulting resistance values were wrong, and the calculated trim resistor R_T failed to balance the bridge. The reason for the failure is probably imprecision in the measurements of R_{M1} through R_{M4}. Incorrect inputs can invalidate the implicit assumptions of Equation (3.24).

The optimal values for R_T were found by direct measurement without mathematical derivation. The bridge was powered with 5 V at V_d. A potentiometer was placed in parallel with each resistive element in turn, and adjusted until the measured potential at the output was zero. The resistance of the potentiometer was then measured and recorded. This trimming method is more labor-intensive but delivers a usable value every time.

3.4 Langmuir Probe

The Langmuir probe is a current-sensing instrument able to bias a surface at a given voltage and measure the current flowing to or from said surface. The bias is provided by a digital-to-analog converter and the current is converted to a voltage by a high performance op amp, configured as shown in Figure 3.4. The op amp is followed by a tunable gain stage.

Using the ideal op amp approximation, a siusoidal current input

$$I_S(t) = A\cos(2\pi f t), \tag{3.28}$$

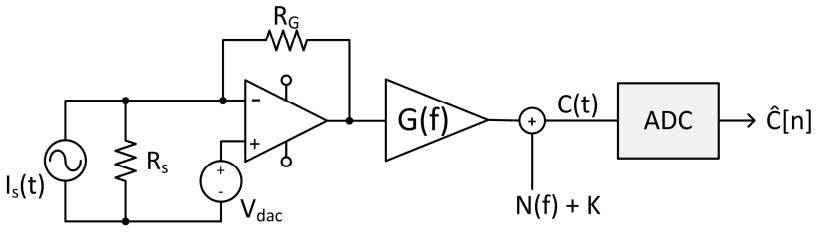

Fig. 3.4: Model of the Langmuir probe.

will have nowhere to go but through R_G, making the signal at the input to the analog-to-digital converter

$$C(t) = (A\cos(2\pi ft)R_G + V_{dac})G(f) + K = A\cos(2\pi ft)R_G G(f) + V_{dac}G(f) + K, \quad (3.29)$$

which can be rewritten for $\hat{C}$ as

$$\hat{C}[t] = A\cos(2\pi fnT)R_G G(f)/Q + (V_{dac}G(f) + K)/Q. \quad (3.30)$$

Equation (3.30) shows a linear relationship, but one slightly different from the linear models for the electric and magnetic field instruments. Here the offset coefficient depends on frequency and DAC voltage. The functional form is

$$\hat{C} = A(f)I_S + B(f)V_{dac} + C. \quad (3.31)$$

The inverse model is

$$I_S = \frac{\hat{C} - B(f)V_{dac} - C}{A(f)}. \quad (3.32)$$

The above models will be the basis for the ASSP calibration. The response of the instruments to known inputs will be recorded, and the data will be fitted to these models.

Chapter 4

Instrument Testing

All seven of the ASSP payloads carry a Langmuir probe, double E-field probe, and 3-axis magnetometer. The main payload also carries a sweeping impedance probe and a multi-bias Langmuir probe dubbed the fast temperature probe. All of these instruments must be carefully tested, not only to verify that they meet specifications but also to calibrate them, so that the PCM count reported by the instrument can be converted to a physical quantity.

Since it is necessary to test many instruments, on many payloads, over a range of temperatures, the total number of testing events is very large. Automating the testing process as much as possible is highly desirable, since each test requires at least one unique wiring configuration, sometimes more. Manually making all these connections for just one payload at one temperature would take a lot of time and introduce a significant risk of human error. This chapter describe the ASSP test plan and the support equipment created to implement it.

4.1 Automation

The desired level of automation for ASSP testing is that a technician can perform a full range of tests on a payload simply by connecting some wires to the payload, clicking start on a computer, and going to lunch. Since different tests call for different wiring configurations, the computer must be able to change the wiring topology without human intervention. This can be achieved by inserting a computer controlled switch relay box between the payload and the test equipment. The testing setup is depicted in Figure 4.1.

Each payload's voltage and current sensing instruments are wired to three signal generators through a switch relay box, (dubbed the testing superbox) and the magnetoresistive

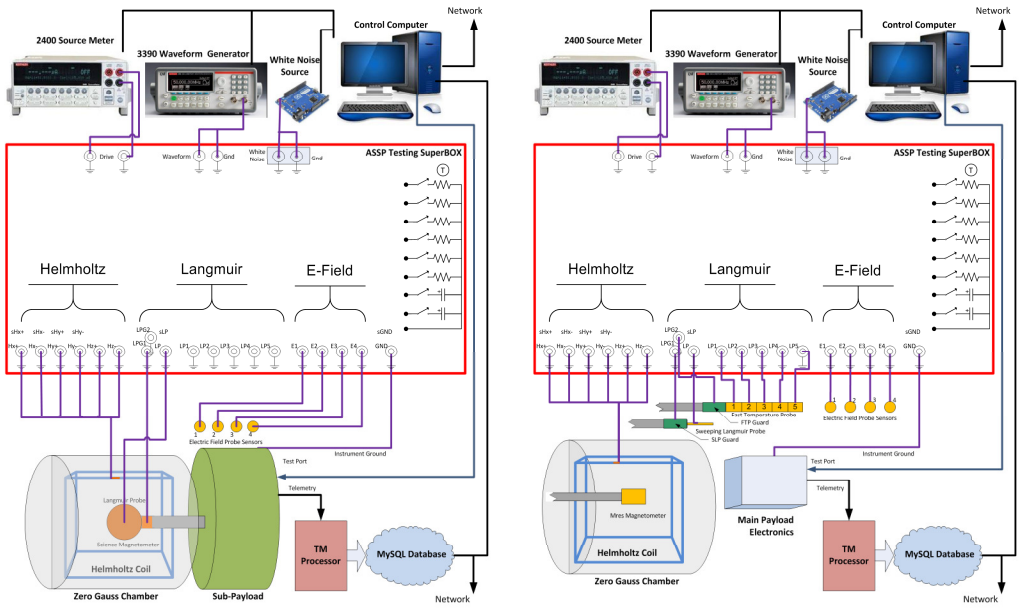

(a) Subpayload (b) Main Payload

Fig. 4.1: Testing physical setup.

magnetometer is mounted at the center of a Helmholtz coil inside a zero gauss chamber. The zero gauss chamber is a small enclosure made of mu-metal, a material with very high magnetic permeability, which serves to isolate the magnetic fields inside the chamber from fields outside of it.

The three signal generators are a Keithley 2400 Source Meter, a Keithley 3390 Arbitrary Waveform Generator, and a custom analog white noise source. The Keithley 2400 and 3390 are documented by the manufacturer. The testing superbox and analog white noise source are described below.

4.1.1 Testing Superbox

The testing superbox is simply a collection of computer controlled switches that can make the connections required for each test without human intervention. The test equipment and payload sensors need only be manually connected to the correct superbox port, at which point the control PC can run any or all of the ten tests. The superbox topology, shown in Figure 4.2 was carefully chosen such that every test's wiring configuration

(described in detail in Section 4.2) can be achieved with the minimum number of physical switches.

The superbox is implemented using two 16-channel optically isolated relay boards made with Huike mini-relays. Each relay board is controlled by an Arduino Leonardo which communicates with a control PC over USB. The innards of the first built superbox are shown in Figure 4.3.

4.1.2 White Noise Source

Figure 4.4 shows a high-level schematic of the circuit that provides the white noise used to test the E-field spectrometer. The noise source is shot noise across the reverse-biased zener diode. Shot noise is noise seen in electrical current as a result of the discrete nature of the charge carriers. In a continuous current a certain average number of electrons are arriving every second. However, the actual number of arrivals in every given second will vary from the average. In general, the size of this sort of statistical fluctuation from the mean is the square root of said mean. The root mean square (RMS) current fluctuation seen in a steady current I is

$$\sigma_i = \sqrt{2qI\Delta f}, \tag{4.1}$$

where q is the elementary charge and Δf is the noise bandwidth.

This current noise is not seen in most applications because of electron-electron interactions. If a larger-than-average number electrons arrive during a given time frame due to random statistical fluctuation, this creates a negatively-charged region which repels "upstream" electrons and thus temporarily reduces the arrival rate. This has the effect of smoothing out the fluctuations due to shot noise in conductors. In resistors and wires shot noise can barely be observed at all. However, shot noise across a p–n junction is not smoothed out by electron-electron interactions because the potential barrier at the junction prevents "downstream" electrons from affecting electrons "above" the junction.

The current noise through the diode becomes voltage noise across the 40K resistor. This voltage signal is amplified by a 3904 bipolar junction transistor (BJT) configured as

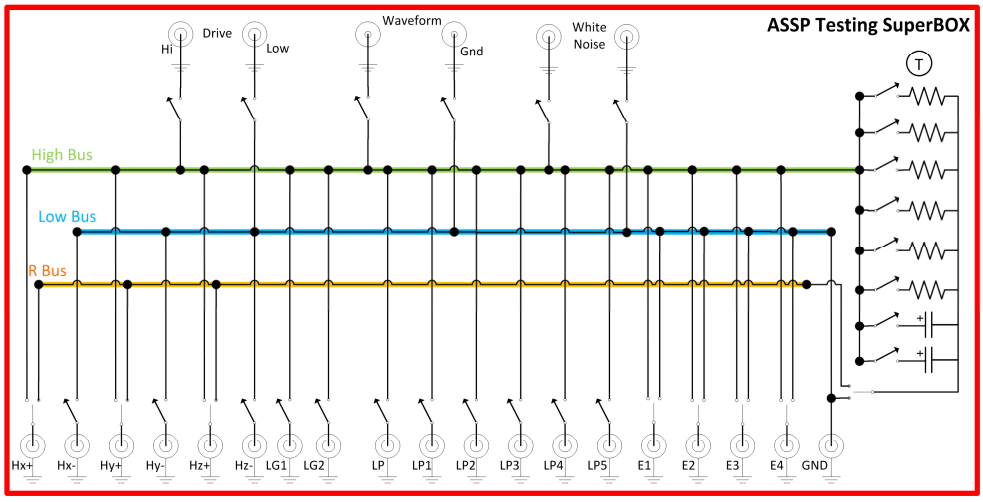

Fig. 4.2: Superbox high-level schematic.

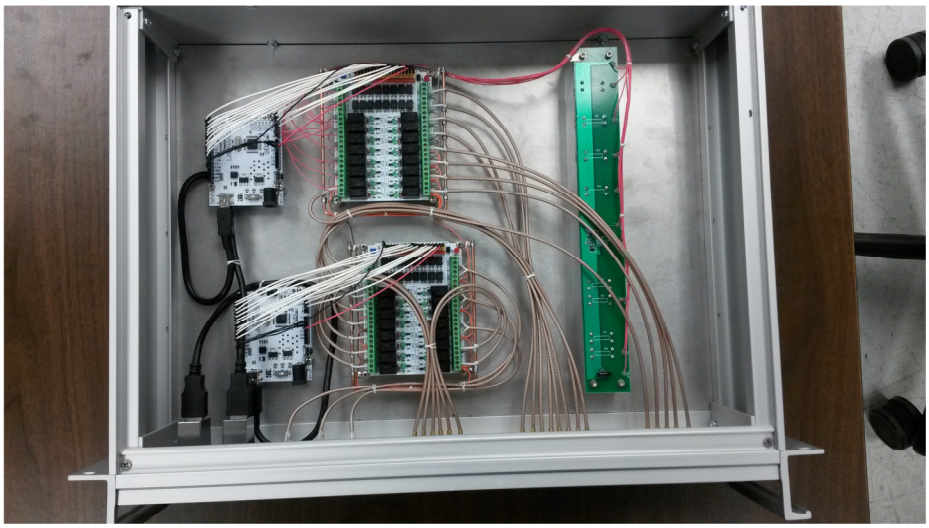

Fig. 4.3: Photograph of a built superbox.

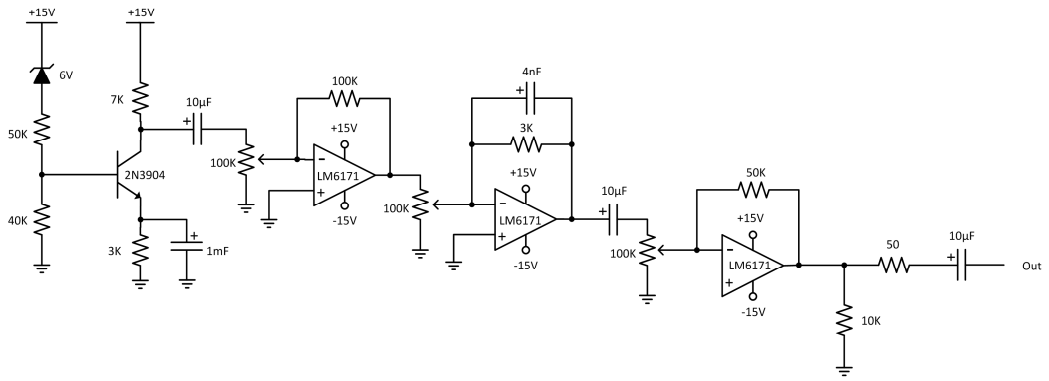

Fig. 4.4: White noise source circuit.

a common emitter amplifier and then three LM6171 op-amps in inverting configurations. A CE BJT is chosen as the first stage because this helps to minimize noise contributed by stages following the first stage [6]. Three 1024 position digital potentiometers along the feedforward paths of the op-amps allow the total gain at the output to range from 0 dB to 140 dB. The capacitor on the feedback path of the second op amp introduces a low-pass filter with a corner frequency of 13 kHz.

The noise seen at the front of the system—the base of the 3904 transistor—is a combination of shot noise and Johnson-Nyquist thermal noise. The RMS thermal voltage noise is

$$v_t = \sqrt{4k_B T R \Delta f} \approx 2.93\mu\text{V}, \tag{4.2}$$

and the RMS voltage shot noise is

$$v_s = \sqrt{2qI\Delta f}R \approx 25.8\mu\text{V}. \tag{4.3}$$

The total noise at the input is the sum of v_t and v_s. It should be noted that since two white noise signals are uncorrelated and therefore orthogonal to one another, they should

be summed using the Pythagorean theorem, rather than simple addition, which gives

$$n_0 = \sqrt{v_s^2 + v_t^2} \approx 26.0\mu\text{V} \approx v_s. \tag{4.4}$$

The equivalent input noise contributed by noises of succeeding gain stages (as shown in Figure 4.5) can be calculated as

$$n = n_0 + \frac{n_1}{G_1} + \frac{n_2}{G_1 G_2} + \frac{n_3}{G_1 G_2 G_3}, \tag{4.5}$$

which, when the proper values are plugged in, yields a total rms noise of

$$n \approx 26.0\mu\text{V} \approx v_s. \tag{4.6}$$

This demonstrates that only about 1% of error will be introduced by neglecting noise sources other than shot noise across the reverse-biased zener diode.

The three op-amps used are the LM6171, chosen because of its large slew rate (3600 V/ µV) and high gain bandwidth product (100 MHz) [7]. The potentiometers are instances of the AD5293, which can tolerate ±15 V and has 1024 wiper positions with 1% accuracy. The AD5293 can accept wiper position commands through a SPI compliant serial bus. An Arduino Leonardo receives commands from a PC and controls the three potentiometers.

Figure 4.6 shows the printed circuit board (PCB) layout used to implement the circuit of Figure 4.4. Power is supplied through three banana plugs and the final signal is sent out via a Bayonet NeillConcelman (BNC) connector. Eight header pins connect to the Arduino

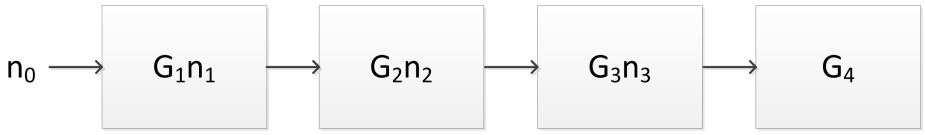

Fig. 4.5: Noise through successive gain stages.

controller.

4.2 Test Plan

This section describes the individual tests which must be performed on each payload. Note that all of these tests must be performed over a range of temperatures, in order to estimate how the calibration coefficients change with temperature. The thermal test plan is depicted in Figure 4.7.

4.2.1 E-field Gain and Offset

This test confirms that the E-field double probe is linear in the ±800 mV/m range, and identifies the gain and offset coefficients needed to convert the raw PCM count to SI units. The E-field probe is connected to the output of a Keithly 2400 Source Meter, with sensors 1 and 3 connected to drive and 2 and 4 connected to ground. The Keithly 2400 sources DC voltage from −8 V to 8 V in 0.25 V steps with 2 second dwell times. The procedure is then repeated with sensors 2 and 4 connected to drive and 1 and 3 connected to ground. The telemetry stream read from the payload during this time is saved in a database.

4.2.2 E-field Frequency Response

This test generalizes the calibration done by the test in Section 4.2.1 to include information about the frequency response of the instrument. The E-field probe is connected to the output of a Keithly 3390 Waveform Generator, with sensors 1 and 3 connected to drive and 2 and 4 connected to ground. The Keithley 3390 outputs a 20 Hz sine wave with amplitude 1 V. After dwelling for 2 seconds the amplitude is set to 0 V for 0.5 seconds. The frequency is incremented on a 20 points per decade schedule, and the process is repeated up to 20 000 Hz. The whole procedure is repeated with sensors 2 and 4 connected to drive and 1 and 3 connected to ground. The telemetry stream read from the payload during this time is saved in a database.

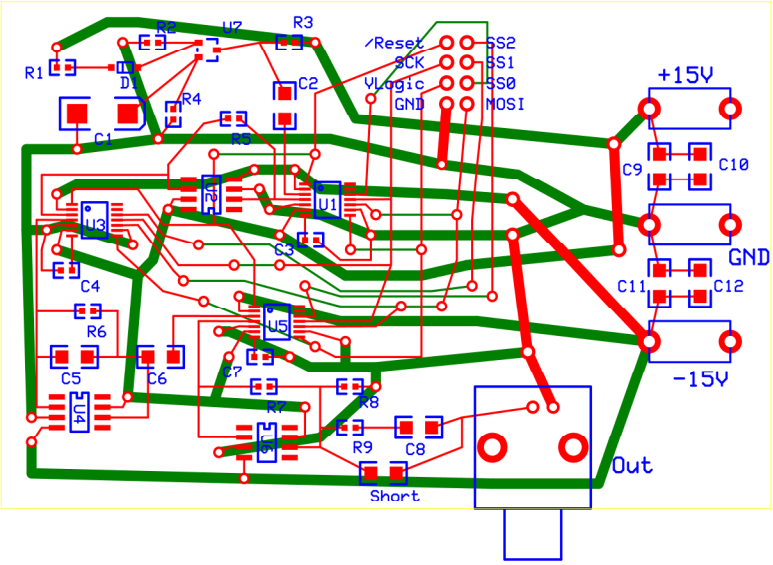

Fig. 4.6: White noise circuit PCB layout.

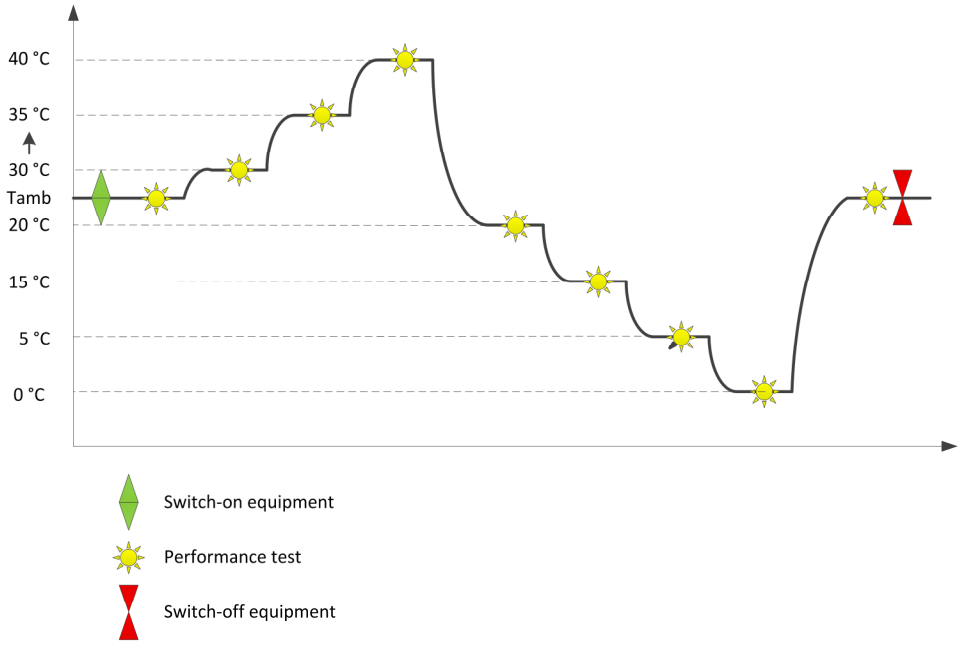

Fig. 4.7: ASSP thermal test plan (courtesy of Julio Martin Hidalgo).

4.2.3 E-field Input Resistance

This test does not create a calibration to be used to interpret science data after flight. Its purpose is to verify that the E-field instrument's input impedance is high enough to satisfy the mission science requirements. E-field sensor 1 is connected to the positive terminal of a 10 pF capacitor, and sensors 2, 3, and 4 are connected to the negative terminal. The Keithly 2400 charges the capacitor to 5 V, and is then disconnected. The whole setup must then be left alone for several minutes while the capacitor slowly discharges through the E-field instrument. The procedure is repeated with sensor 2 connected to positive and 1, 3, and 4 connected to negative, then with sensor 3 connected to positive and 1, 2, and 4 to negative, and finally with sensor 4 connected to positive and 1, 2, and 3 connected to negative. The telemetry stream read from the payload during this time is saved in a database.

4.2.4 E-field Spectrometer Frequency Response

This test determines the exact frequency range each spectrometer bin is sensitive to. The procedure is identical to the test described in Section 4.2.2. Only the postprocessing is different.

4.2.5 E-field Spectrometer White Noise Response

This test identifies the gain an offset coefficients needed to convert PCM counts reported by the spectrometer to SI units of power and amplitude spectral density. The E-field probe is connected to the output of a custom-built white noise source, with sensors 1 and 3 connected to drive and 2 and 4 connected to ground. The white noise source is set to a PSD of 1×10^{-14} V^2/Hz for 5 seconds, then to zero for 1 second. The PSD is incremented by one point per decade and the process is repeated up to 1×10^{-3} V^2/Hz. The whole procedure is repeated with sensors 2 and 4 connected to drive and 1 and 3 connected to ground. The telemetry stream read from the payload during this time is saved in a database.

4.2.6 Magnetometer Gain and Offset

This test confirms that the science magnetometer is linear in the ±50 000 nT range, and identifies the gain and offset coefficients needed to convert the raw PCM count to nanotesla. The magnetometer is positioned at the center of a Helmholtz coil in a zero-gauss chamber. The Helmholtz coil's x axis is connected to a Keithley 2400. The Keithley 2400 sources current such that the magnetic field generated by the Helmholtz coil is −50 000 nT. The field is increased to 50 000 nt in 40 steps with 2 second dwells. The procedure is repeated for each axis and combination of axes: x, y, z, xy, xz, yz, xyz. The telemetry stream read from the payload during this time is saved in a database.

4.2.7 Magnetometer Frequency Response

This test generalizes the calibration done by the test in Section 4.2.6 to include information about the frequency response of the instrument. The magnetometer is positioned at the center of a Helmholtz coil in a zero-gauss chamber. All of the Helmholtz coil's axes are connected to a Keithley 3390. The 3390 outputs a 10 Hz current signal such that the magnetic field amplitude is 100 nT for 2 seconds. The current amplitude is then set to zero for 0.5 seconds. The frequency is incremented on a 20 points per decade schedule, and the process is repeated up to 10 000 Hz. The process should then be repeated with magnetic field amplitude 10 000 nT. The telemetry stream read from the payload during this time is saved in a database.

4.2.8 Langmuir Probe Gain and Linearity

This test confirms that the high and low gain channels of the subpayload Langmuir probe range, main payload sweeping Langmuir probe, and fast temperature probe are linear in their respective regions, and identifies the gain and offset coefficients needed to convert the raw PCM count to amperes. The Langmuir probe is connected to a Keithley 2400. The Langmuir probe DAC is set to −3 V .The Keithley outputs both positive and negative DC current at the magnitudes listed in Table 4.1, with one second dwells. The process is repeated for DAC voltages of zero V and 3 V. The telemetry stream read from the payload

during this time is saved in a database.

The subpayload Langmuir probe is tested just as described above, but the main payload Langmuir probes must be tested one at a time. The above procedure must be repeated six times, for the SLP and each surface of the FTP.

4.2.9 Langmuir Probe Precision Gain and Linearity

This test produces a finer measurement of the Langmuir probe gain and offset coefficients by drawing current through precision resistors rather than from a source meter. It also measures the true voltage that the DAC is producing at each of its settings. The Langmuir probe is connected to ground through a high precision 7 MΩ resistor. The DAC is swept through its full range. The procedure is repeated for resistor values 1.5 MΩ, 250 kΩ, 2.5 kΩ, 1 kΩ, and 350 Ω. The Langmuir probe is then disconnected from any resistors. The electric field instrument is connected up, with probes 1 and 3 connected to the Langmuir probe guard and 2 and 4 connected to ground. The DAC is once more swept through its full range. The telemetry stream read from the payload during this time is saved in a database.

For the main payload, the entire above process must be repeated for the SLP and each surface of the FTP.

4.2.10 Langmuir Probe Frequency Response

This test generalizes the calibration done by the test in Section 4.2.8 to include information about the frequency response of the Langmuir probe. The Langmuir probe is connected to a Keithley 3390 through a 2.5 kΩ resistor, and the DAC is set to zero volts.

Table 4.1: Current steps for Langmuir probe testing.

Instrument Range	Current Steps	Units
Main SLP-H	0, 5, 10, 15, 20, 25, 30, 35, 40	nA
Main FTP-H	50, 100, 150, 200, 250	nA
Sub LP-H	300, 350, 400, 450, 500, 550, 600	nA
Main SLP-L	2, 4, 6, 8, 10, 12	µA
Main FTP-L	20, 30, 40, 50, 60	µA
Sub LP-L	70, 80, 90, 100, 110, 120	µA

The 3390 outputs a voltage sine wave with amplitude 0.25 V and frequency 10 Hz for 2 seconds. This results in a sinusoidal current with amplitude 100 µA flowing through the resistor and into the Langmuir probe. The voltage amplitude is then set to zero for 0.5 seconds. The frequency is incremented on a 20 points per decade schedule, and the process is repeated up to 10 000 Hz. The telemetry stream read from the payload during this time is saved in a database.

Chapter 5

Future Tasks

Delays in the overall ASSP mission timeline have made it impossible for the instrument calibration to be completed by Spring 2014. This thesis has been written as a reference to be used by those who will finish the implementation of the ASSP test plan. The important tasks yet to be done are described below.

Calibrations must be created for the Helmholtz coil and the white noise source. These calibrations will be fairly straightforward to generate, but have not been done because important parts have not yet been built.

The calibration of the Helmholtz coil will convert the current flowing through each coil to field strength in the corresponding axis at the center of the coil when the coil is in the back of the zero gauss chamber. It will use a linear model for each axis.

The calibration of the white noise generator will convert the wiper settings of the three digital potentiometers to a power or noise spectral density. Rather than use a mathematical model in this calibration, it is proposed that the experimenter should use trial and error to identify a setting which delivers each of the roughly 15 desired noise magnitudes. This will take a moderate amount of time, but will result in unambiguous settings for the noise output.

Arduino code to control the white noise circuit must be written. The arduino need only receive three wiper positions from the control pc and write them to each digital potentiometer in turn. There is working code which writes a wiper position to a digital potentiometer, so all that really needs to happen is for this code to be integrated into a modified version of the superbox arduino code.

Control scripts that automate each test procedure must be written. Communication with the test equipment is well documented and working so it should be straightforward.

Section 4.2 of this thesis should be helpful.

Calibration scripts that analyze the test data and generate forward and backward model coefficients according to the theory developed in Chapter 3 must be written. This is the most significant item in terms of ability and time needed.

References

[1] N. Ivchenko, G. Marklund, K. Lynch, D. Pietrowski, R. Torbert, F. Primdahl, and A. Ranta, "Quasiperiodic oscillations observed at the edge of an auroral arc by auroral turbulence 2," *Geophysical Research Letters*, vol. 26, no. 22, pp. 3365–3368, 1999. [Online]. Available: http://dx.doi.org/10.1029/1999GL003588

[2] K. A. Lynch, D. Pietrowski, R. B. Torbert, N. Ivchenko, G. Marklund, and F. Primdahl, "Multiple-point electron measurements in a nightside auroral arc: Auroral turbulence ii particle observations," *Geophysical Research Letters*, vol. 26, no. 22, pp. 3361–3364, 1999. [Online]. Available: http://dx.doi.org/10.1029/1999GL900599

[3] Y. Zheng, K. A. Lynch, M. Boehm, R. Goldstein, H. Javadi, P. Schuck, R. L. Arnoldy, and P. M. Kintner, "Multipoint measurements of field-aligned current density in the auroral zone," *Journal of Geophysical Research: Space Physics*, vol. 108, no. A5, 2003. [Online]. Available: http://dx.doi.org/10.1029/2002JA009450

[4] E. T. Lundberg, P. M. Kintner, K. A. Lynch, and M. R. Mella, "Multi-payload measurement of transverse velocity shears in the topside ionosphere," *Geophysical Research Letters*, vol. 39, Jan. 12 2012.

[5] K. A. Lynch, D. Hampton, M. Mella, B. Zhang, H. Dahlgren, M. Disbrow, P. M. Kintner, M. Lessard, E. Lundberg, and H. C. Stenbaek-Nielsen, "Structure and dynamics of the nightside poleward boundary: Sounding rocket and ground-based observations of auroral electron precipitation in a rayed curtain," *Journal of Geophysical Research: Space Physics*, vol. 117, no. A11, 2012. [Online]. Available: http://dx.doi.org/10.1029/2012JA017691

[6] J. Leach, W.M., "On the calculation of noise in multistage amplifiers," *Circuits and Systems I: Fundamental Theory and Applications, IEEE Transactions*, vol. 42, no. 3, pp. 176–178, Mar. 1995.

[7] *LM6171 High Speed Low Power Low Distortion Voltage Feedback Amplifier*, Texas Instruments, May 1998, LM6171 datasheet.

Appendix

The appendix is not so much this text as a DVD which contains primary and supplementary information about this thesis work, as well as some other work done by the writer of this thesis, but not documented in the thesis itself. The DVD contains the following folders:

ASSP Test Plan

Contains diagrams and slideshows which help describe and define the automated test plan and the superbox.

ExpressPCB

Contains schematic and layout files for the custom white noise circuit described in Chapter 4.

Magnetic Contamination

Contains Powerpoint and Excel files describing and implementing an approach to characterizing the magnetic field due to the ASSP subpayload seen at the ASSP subpayload magnetometer.

Magnetometer Trimming

Contains documents used during the magnetometer trimming process described in Chapter 3, as well as reports on the resistors attached to each device.

MATLAB

Contains all the matlab scripts used to optimize the ASSP ejection, as well as the derived data products.

Posters

Source files for the ASSP posters displayed at the American Geophysical Union fall meeting in 2012 and 2013.

Presentations

Powerpoint slideshows describing the thesis work.

Thesis

Latex source for this very document.

Thesis Proposal

Latex source for the thesis proposal.